

Electrical and Optical Discharge Studies with various MPGDs

Bachelor Thesis

Scientific thesis to obtain the degree

B.Sc.

at the Department of Physics of the Technical University München.

Supervised by

Prof. Dr. Laura Fabbietti

Dense and Strange Hadronic Matter (E62)

Submitted by

Tobias Waldmann

Grasmeierstraße 25

80805 München

Submitted at

München, 26. Oktober 2020

Authorship

I confirm that this bachelor thesis in physics is my own work and I have documented all sources and materials used.

München, 26. Oktober 2020, Signature

Contents

Introduction	9
1 Micro Pattern Gaseous Detectors	11
1.1 Working Principle	11
1.2 Micromegas	12
1.3 GEMs	13
2 Discharges in MPGDs	15
2.1 Micromegas	16
2.2 (TH)GEMs	16
3 Electrical Discharge Studies with Micromegas	19
3.1 Experimental Setup	19
3.2 Measurement Procedures	23
3.3 Results	24
4 Optical Discharge Studies with (TH)GEMs	35
4.1 Experimental Setup	35
4.2 Measurement Procedures	38
4.3 Results	41
5 Summary and Outlook	49
Acknowledgements	51

List of Figures

1.1	Working principle of MPGDs.	12
1.2	Simulated field lines in Micromegas.	13
1.3	Simulated field lines in GEMs.	13
2.1	Primary discharge vs. secondary discharge vs. electron avalanche.	16
2.2	Electric signal of primary and secondary discharges.	17
3.1	Scheme of the Micromegas detector setup.	19
3.2	Picture of the Micromegas detector setup.	20
3.3	Energy spectrum of the mixed alpha source.	21
3.4	Simulated Bragg curves of the alpha particles for different gas mixtures.	22
3.5	Micromegas 1 gain measurements.	25
3.6	Micromegas 1 gain measurements (sorted by gas).	26
3.7	Comparison of Micromegas 1 and 2 gain measurements.	26
3.8	Micromegas 1 discharge probability.	27
3.9	Micromegas 2 discharge probability.	28
3.10	Micromegas 1 discharge probability (sorted by gas).	29
3.11	Micromegas 2 discharge probability (sorted by gas).	30
3.12	Comparison of discharge probability for both Micromegas (sorted by gas).	31
3.13	Ion backflow of both Micromegas.	33
4.1	Scheme of the spectroscopy detector setup.	36
4.2	Pictures of the different "exotic" sh-THGEMs.	37
4.3	Wavelength calibration.	39
4.4	Intensity calibration.	39
4.5	Background fit and subtraction.	40
4.6	Comparison of background for Ar 100 and Ar-CO ₂ 90-10.	41
4.7	Cu GEM spectrum in Ar-CO ₂ 90-10.	42
4.8	Comparison of Cu and Al GEM spectra in Ar-CO ₂ 90-10.	43
4.9	Comparison of GEM and sh-THGEM spectra for Al and Cu.	44
4.10	Spectra of all six sh-THGEMs.	45
4.11	Secondary emission spectrum.	45
4.12	Secondary discharge probability of sh-THGEMs.	47

List of Tables

3.1	Characteristic energies of alpha particles.	20
3.2	Relevant gas properties.	22
4.1	Relevant material properties.	37
4.2	Primary discharge onset voltages.	42

Introduction

In the wide range of micro pattern gaseous detectors, two distinct types stand out due to their performance and usability: Micromegas and Gas Electron Multipliers (GEMs). Both are used in large high-energy physics experiments, like ATLAS and ALICE or CAST and COMPASS. In general, they are able to reliably detect a large variety of ionizing particles. However, there are of course operational limits, where this reliability ends. In this thesis, different aspects of the performance of MPGDs in these boundary regions are investigated and studied.

In the first part of these studies, characterizations are done on two Micromegas samples, using already established measurement procedures and concepts like gain, discharge probability, or ion backflow. These parameters, which hugely influence the operational stability at high gains and particle rates, are crucial factors for the efficiency of Micromegas in modern particle physics detectors. The conducted measurements give further insights into the gain and discharge stability, especially looking at dependencies concerning the used gas. For this, the two Micromegas with slightly different geometries were tested regarding their performance, using four different gas mixtures.

In the second part, a new, unconventional approach was taken to study the discharge phenomenon in GEMs. More precisely, spectroscopy methods were used to take a closer look at the light emitted during these events. Discharges can occur during high gain operation, potentially blinding and even damaging the GEM foil and its connected electronics, limiting the optimal stable performance of the detector. Over the years, a lot of research and progress regarding discharge prevention and mitigation was made. But up till today, some major questions concerning their formation mechanism remain unanswered. This is where spectroscopy excels as a useful tool to study the effect of various "exotic" GEM foil materials on light emitted during discharges. With this, new insights into the formation mechanism of these discharge events in GEMs are obtained.

Chapter 1

Micro Pattern Gaseous Detectors

One of the simplest kinds of gaseous ionizing detectors is the ionizing chamber, a gas-filled box with two parallel plates inside and an electric field between them. A particle going through the chamber will ionize the gas and create electron-ion pairs along its trajectory. The liberated electrons drift towards the anode due to the applied field, inducing a signal. However, the electric signals created through direct ionization of the gas mixture are not sufficient for high energy particle physics. Thus a signal amplification has to take place. A major advancement regarding proportional amplification in high-rate particle detectors was made about 50 years ago with the development of multi-wire proportional chambers [1], where electron avalanche amplification takes place near anode wires due to the modified, stronger electric field. **Micro Pattern Gaseous Detectors** (MPGD) are the newest addition, effectively replacing the wires with micro patterned structures. They offer major improvements like intrinsic ion back flow suppression, resulting in a higher detector rate capability [2, 3], as well as increased energy and spatial resolution [4]. There are many different types of MPGDs and even more subtypes, only differing slightly in geometric properties, used materials, or production methods, but all of them follow the same working principle.

1.1 Working Principle

This thesis focuses on two different MPGD types, namely Micromegas [5] and Gas Electron Multipliers (GEMs)[6]. The setup itself is relatively simple, consisting of a cathode, the micro patterned amplification stage, and an anode to read out the received signals. While the concept of cathode, drift volume, and readout anode is similar for both Micromegas and GEMs, the amplification stage is the major difference. In figure 1.1 a simplified scheme of such a detector is shown.

The region between the cathode and the amplification stage is called drift volume, where a constant electric field is applied, named drift field. This is where the primary ionization of the gas mixture through ionizing particles takes place. The generated electron-ion pair can overcome its mutual attraction due to the applied drift field, causing them to drift apart. While the heavy ions slowly get collected on the cathode, the electrons quickly drift towards the amplification stage. In this region, electrons get accelerated even more, due to the special geometry of the micro patterned structures and higher applied electric fields. When the resulting field is strong enough, the electrons are able to ionize further gas atoms, creating more electrons and eventually resulting in a so-called electron avalanche

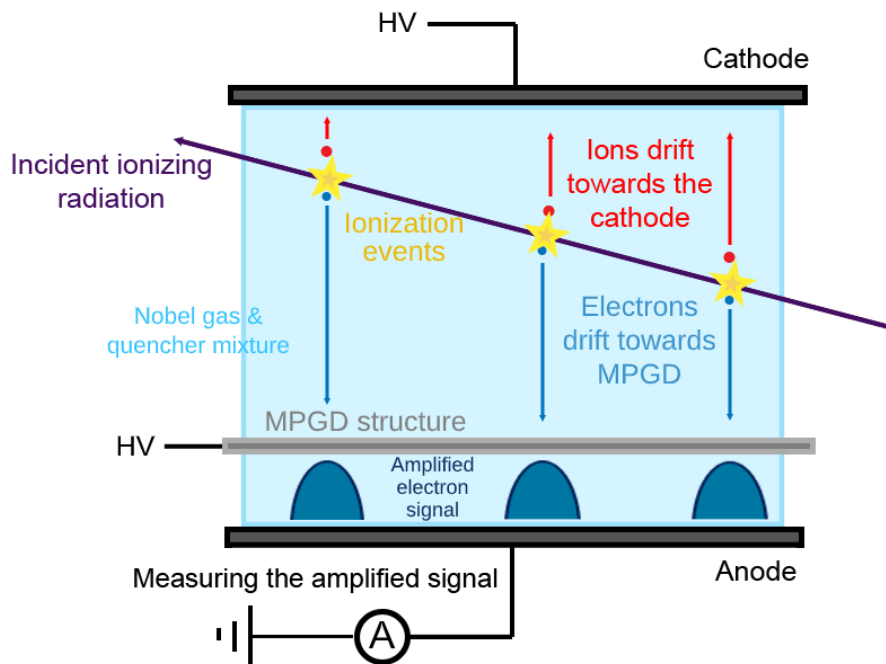


Figure 1.1: Scheme showing the working principle of MPGDs. Ionizing particles create electron-ion pairs in the drift volume between cathode and MPGD structure. Due to the applied drift field, electrons drift towards the structure while ions get collected on the cathode. In the amplification stage, including the MPGD structure, very high amplification fields are applied, causing electron avalanche multiplication. These amplified electric signals get readout on the anode.

[1]. This accumulation of electrons then drifts towards the anode, where the enhanced electric signal gets measured by readout electronics.

1.2 Micromegas

Micro Mesh Gaseous Structures (Micromegas) are the first type of such MPGDs studied in this thesis. They were developed in 1992 by I. Giomataris and G. Charpak [5], initially originating from parallel plate detectors used in Hadron Blind Detector experiments. These were modified with a smaller amplification gap to speed up signal recording [7]. Showing huge improvements, different subtypes of Micromegas were developed and implemented in many experiments, like CAST [8], COMPASS [9] or NA48 [10] throughout the years. Micromegas are still used up till today and were, for example, just currently implemented into the ATLAS New Small Wheel detector for muon detection [11].

In Micromegas, the amplification takes place between the micro mesh and the readout anode by applying a high potential difference, resulting in a strong electric field. In figure 1.2 the micro mesh, the anode, and a simulation of the electric field configuration are shown. Looking at the electric field lines, it becomes clear, that electrons from the drift volume follow the field lines and enter the amplification region. As only small transversal diffusion effects affect the path of the electrons, an electron transmission transparency of nearly 100% is achieved [13]. In return, the ions created in the amplification region through avalanche processes are collected on the micro mesh, resulting in a relatively low ion backflow (IBF) [2]. This is important, as ions inside the drift volume distort the electric field configuration, disturbing the spatial resolution of the detector.

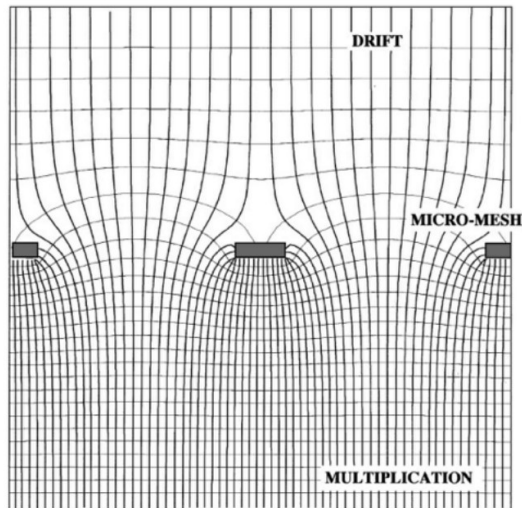


Figure 1.2: Simulation of electric field lines around the micro-mesh structure, showing the different strengths of drift and amplification field. Looking at the field lines, the high electron transparency as well as the low ion backflow become clear. [12]

1.3 GEMs

Gas Electron Multipliers (GEM) are the second type of MPGDs, invented by Fabio Sauli 1997 [6]. They have been implemented in a wide range of major experiments like COMPASS [14], LHCb [15], TOTEM [16] or the upgraded ALICE TPC [17].

The amplification follows the same principle as in Micromegas, but the way the strong electric field is achieved differs. In figure 1.3 a scheme of a standard GEM foil is shown, again including simulated field lines [18]. The electron multiplication takes place inside the GEM holes between the top and bottom electrodes. The required strong electric fields are achieved due to the special hole geometry. Additionally, a so-called induction field is applied between the bottom GEM electrode and the anode, causing the before created electron cluster to drift towards the anode.

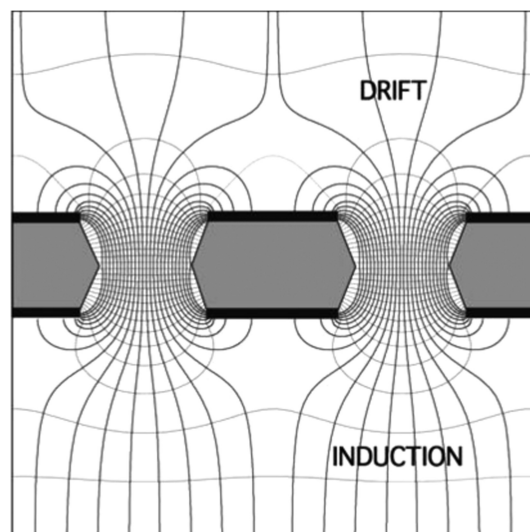


Figure 1.3: Simulation of the electric field lines around the GEM holes. The different field strengths of drift field, amplification field inside the holes, and induction field are shown. [18]

THGEMs

A slightly modified version of GEMs are the so-called **Thick** GEMs (THGEM) [19]. While the working principle stays the same, its dimensions are expanded by a factor of 5-20, resulting in larger holes and thicker cladding. This makes production much easier, as holes now get mechanically drilled and the thicker Kapton layer enables larger active detector areas without supportive structures [20]. Due to their dimensions, THGEMs are more robust against radiation and electrical discharges [21], but in turn, also show a lower discharge stability [22]. However, this makes them a perfect tool for high rate discharge studies. When talking about GEMs and THGEMs simultaneously, (TH)GEM will be used as an abbreviation for the rest of the thesis.

Chapter 2

Discharges in MPGDs

One of the major limiting factors for high gain operations with MPGDs are electrical discharges [23]. Discharges are breakdown events occurring inside the amplification structure, causing high current flow and may temporarily or permanently blind or even damage the detector. As a consequence, it is of crucial importance to prevent or at least mitigate discharges and their impact. Throughout the years, numerous strategies for mitigation were developed. This includes optimizations of the high voltage system [24], the addition of resistive layers to parts of the MPGDs [25], as well as segmenting of the micro patterned amplification structures [24]. Further, stacking of MPGDs leads to lower individual electric fields while still reaching the same total gain, thus also increasing the overall discharge stability [25].

Besides their mitigation, also the physics behind the formation mechanism of discharges have been extensively studied [23, 24]. The general process leading to a discharge is similar for both MPGDs. Through the avalanche process in the amplification region, electron-ion pairs are created. While the electrons drift towards the bottom amplification electrode, either being the anode for Micromegas or the bottom layer of (TH)GEMs, the ions slowly drift back to the top electrode. These spacial separated charges, named space charge, modify and increase the local electric field. When this enhancement of the amplification field becomes strong enough, a so-called streamer discharge forms [26], possibly creating a conductive tunnel between the top and bottom electrodes. Eventually, this causes a drop in the potential difference across the amplification gap, thus quenching the further development of the spark.

In general, discharge formation depends on the charge density inside the amplification region exceeding a certain limit. One possible way to reach this limit is to enhance the avalanche multiplication by increasing the respective potential difference. However, also an increased amount of primary electrons from the initial ionization process leads to more charges created through multiplication, thus inducing discharges. This is influenced by the used gas mixture, as the charge densities created along the path of the ionizing particles depend on gas specific properties. Further, also the path itself plays a role, as electrons created by particles passing the drift volume perpendicular to the micro patterned amplification structures will eventually end up in the same region, thus hugely increasing the respective charge density.

While the processes are similar, the overall stability against discharges differs for both MPGDs due to their different geometries.

2.1 Micromegas

In Micromegas, the streamer discharge develops between the micro mesh and the anode. However, its dependence on the geometry and the used gas mixture is not fully understood so far. Experiments and simulations with parallel plate geometries showed a dependency on the charge density in the amplification gap [27]. This would therefore point to a dependency on the used gas mixture and some of its specific properties, also for Micromegas. On top of that, two-dimensional simulations of two single wires showed that lower wire distances result in higher maximal achieved electric amplification fields, eventually decreasing the discharge stability [28]. In comparison to that, properties of the mesh, such as wire thickness and density were observed to influence the achievable gain as well as the stability against discharges [29]. Meshes with higher wire density and thinner wires showed better performances, presumably due to more uniform electric fields. In general though, Micromegas are relatively easy to discharge, as these are for example heavily influenced by dust particles [30]. Even small single point defects on the mesh wires can heavily influence the discharge stability [28]. To improve the understanding of discharges and their dependencies on gas and mesh geometry, a more in-depth study regarding discharge stability is presented in this thesis (see chapter 3).

2.2 (TH)GEMs

In (TH)GEMs, two different kinds of discharges have to be distinguished. The primary discharges, developing inside the (TH)GEM holes and the so-called delayed secondary discharges, occurring in the induction gap. The formation mechanism of the former ones is quite well understood. The streamer discharge forms inside the holes of the (TH)GEM foil, as the space charge is built up between the top and bottom (TH)GEM electrodes. It was shown, that the total charge inside the holes is the main reason for the field enhancement causing the discharge formation. In comparison to the Raether limit in parallel plate detectors [31], critical charge limits were found for GEMs [32], as well as THGEMs [22]. Additionally, a dependency on the used gas mixture and the hole geometry was observed.

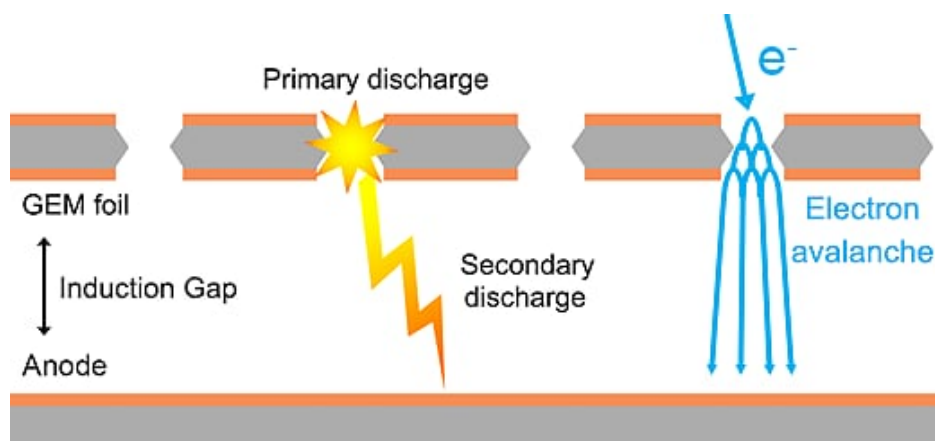


Figure 2.1: Scheme showing the spatial differences between primary and secondary discharges in a GEM detector. While primary discharges form inside the GEM holes, secondaries develop in the induction gap between the bottom GEM electrode and the anode. An electron avalanche is shown as a reference.

The formation mechanism behind secondary discharges is not really understood so far. They develop as a propagation of a primary discharge in the induction gap between the bottom (TH)GEM electrode and the anode. A scheme clarifying the spatial differences

between primary and secondary discharges is shown in figure 2.1. However, the applied field strength in this region is way too low to cause standard streamer discharges. Furthermore, a relatively large time delay (1 μs to 100 μs) is observed between primary and secondary discharges, as depicted in figure 2.2. This also rules out fast discharge formation mechanisms like increased ionization due to UV photon emission from the preceding primary spark. One of the leading theories so far is the so-called thermionic electron emission. It assumes, that the heat created during a primary discharge is high enough to cause the ejection of electrons from the foil material [33, 34]. These thermionic electrons then again modify the local induction field and cause a discharge to form. Although this can explain the time delay, the same secondary discharge behavior was observed with an inverted induction field, thus pointing to yet unknown phenomenons. As some questions remain unanswered, the latter part of this thesis (see chapter 4) takes a new optical approach to study the effect of foil material on secondary discharge formation.

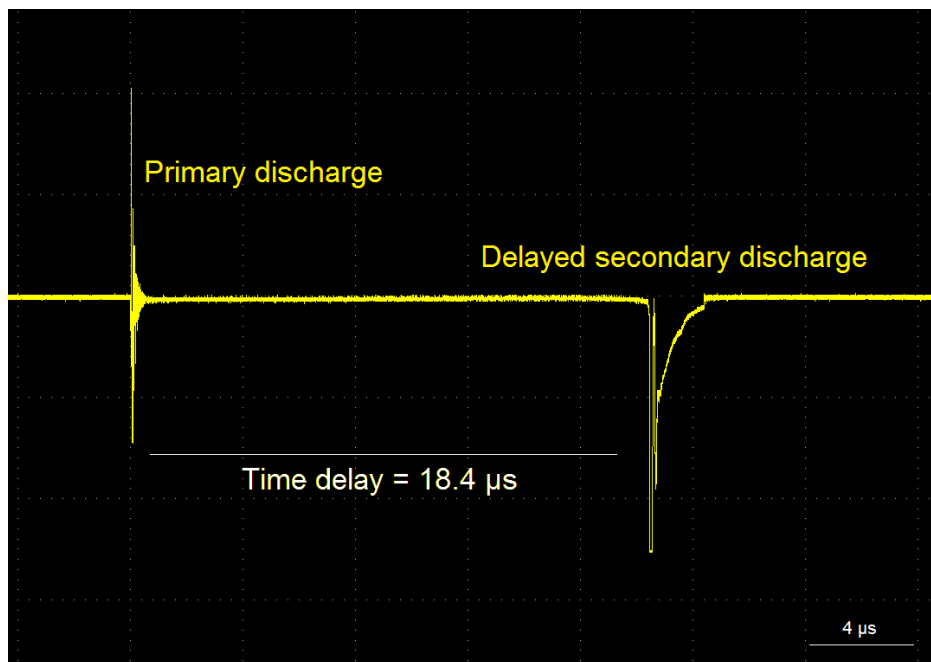


Figure 2.2: Electrical signal of a primary discharge, followed by a delayed secondary discharge. The large time delay, as well as the different shapes, can be seen.

Chapter 3

Electrical Discharge Studies with Micromegas

3.1 Experimental Setup

For the Micromegas studies, a dedicated detector chamber was used. It consists of a gas-tight box, containing supportive structures where the cathode and the Micromegas are mounted on. The provided Micromegas are produced as a compact bulk, including the woven steel micro-mesh itself as well as the single plane readout anode, mounted on a 1.5 mm thick PCB plate. A scheme of the setup is shown in figure 3.1.

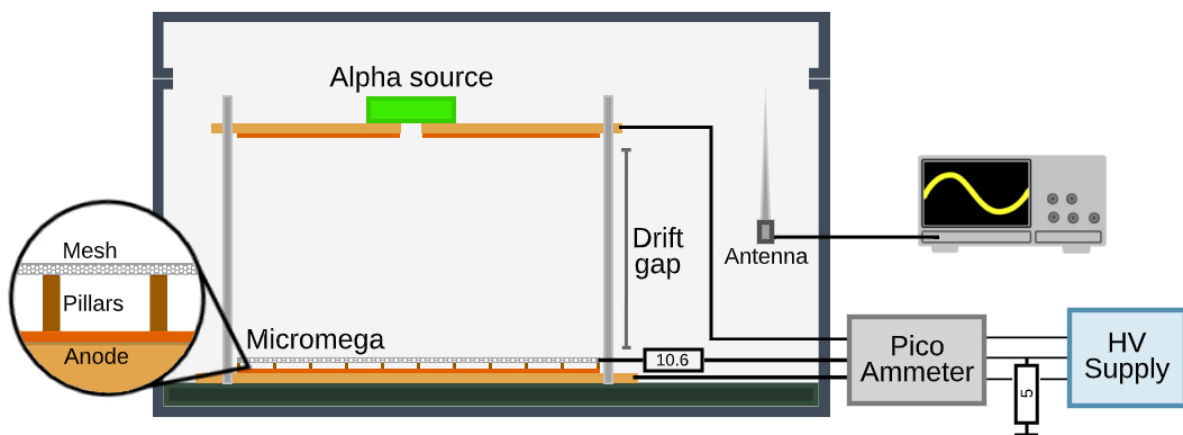


Figure 3.1: Scheme of the detector chamber for the stability studies with Micromegas. Cathode and Micromegas, consisting of mesh and anode, are mounted on a support structure. The mixed alpha source is placed on top of the cathode. High voltages can be applied to all three electrodes, while their currents are read out. An antenna is used to detect the electric signals created by discharges.

A multi-channel high-voltage power supply is connected to the three electrodes, with the connection to the micro mesh including a 10.6 MΩ protection resistor. In addition, a 5 MΩ grounding resistor is attached as protection against trips in the power supply. A PicoLogic PA125-24 pico-ammeter module is used to read out the currents flowing through the three channels. Further, a fourth channel is connected to an antenna inside the detector chamber, used to detect the electrical signals caused by discharges. These signals are then measured and counted with an oscilloscope.

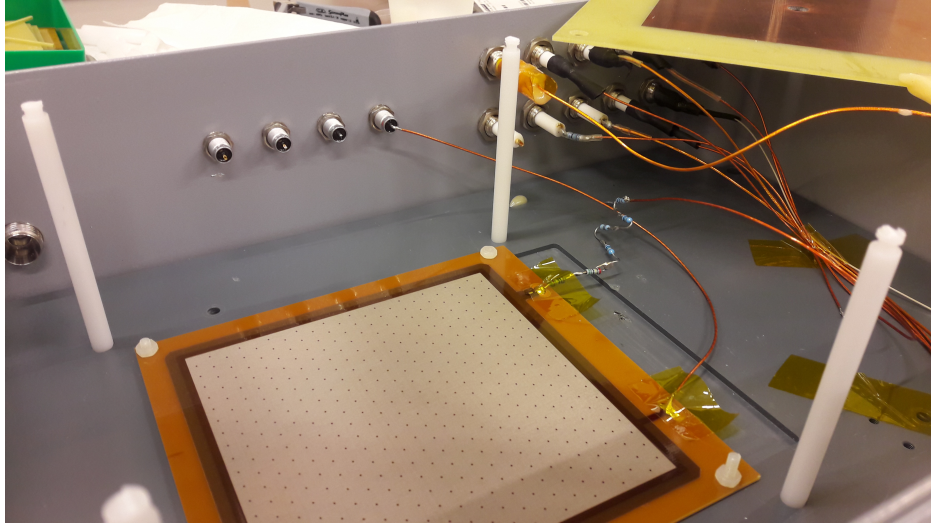


Figure 3.2: Picture of Micromegas 1 integrated into the detector chamber. The dismantled cathode can be seen in the top right corner, above the connections for power supply, readout electronics, and antenna.

Two different Micromegas with an active area of 10 cm x 10 cm were produced at CERN and provided for this thesis. The picture in figure 3.2 shows Micromegas 1 built-in into the detector chamber. The cathode is dismantled but can be seen in the top right corner. The amplification gaps are fixed at 128 μm . To ensure a constant gap across the whole mesh structure, pillars were placed as space holders in a hexagonal pattern between the anode and the mesh.

Micromegas 1 and 2 have different mesh geometries, 640/15 and 730/13 respectively. The first number describes the number of wires per inch (LPI), effectively a wire density, while the second number relates to the wire thickness in μm . The drift distance was varied throughout the conducted measurements, the drift field however was kept constant at 400 V/cm.

Radiation Source

Radionuclide	Energy [MeV]	Intensity [%]
^{239}Pu	5.105	11.5
	5.143	15.1
	5.55	73.4
^{241}Am	5.388	1.4
	5.442	12.8
	5.486	85.2
^{244}Cm	5.763	23.3
	5.805	76.7

Table 3.1: Characteristic energies and relative intensities of the emitted alpha particles. Only the most intense particles of the three different source components, ^{239}Pu , ^{241}Am , and ^{244}Cm are shown. [35]

As supply for ionizing particles, a mixed ($^{239}\text{Pu} + ^{241}\text{Am} + ^{244}\text{Cm}$) alpha source with a diameter of 25 mm and a height of 0.5 mm is used. The diameter of the active area measures 7 mm, thus, a similar-sized hole is provided in the center of the 1.5 mm thick

PCB plane of the cathode, enabling the irradiation of the drift volume. The different characteristic energies of the emitted particles are listed in table 3.1.

In figure 3.3 the energy distribution of the used alpha source is shown. It was measured with Micromegas 2 in Ar-CO₂ 90-10. The background noise is seen in the low energy region, while the three observed peaks can be associated with the respective source components. However, the energy resolution is not good enough to distinguish between different characteristic energies of a single nuclide. By integrating over the total distribution, excluding the low energy background, the rate of the source can be calculated. It yielded a rate of (477.2 ± 0.8) Hz.

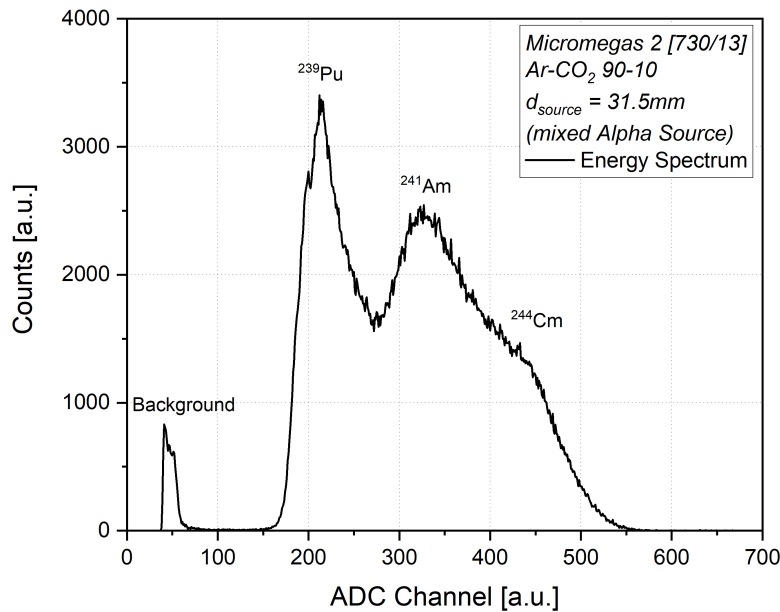


Figure 3.3: Energy spectrum of the mixed alpha source, measured with Micromegas 2 in Ar-CO₂ 90-10 at a source distance of $d_{\text{source}} = 31.5$ mm. The background noise can be seen in the low energy region, while the three peaks in the main part can be assigned to the three different nuclides.

Gas

A Bronkhorst gas distribution system is used to flush the detector chamber with different gas mixtures, providing a constant exchange of the gas. The flushing rate was set to $10^{-3} \text{ m}^3/\text{h}$ minimizing the contamination with O₂ and H₂O (humidity), as well as ensuring a constant overpressure of 4 mbar with respect to the ambient pressure. This is important, as the humidity was shown to hugely influence the discharge stability of a parallel plate setup [27]. Although Micromegas are different from parallel plate detectors, a similar behavior can be expected and was also observed throughout our measurements, but no further systematic studies were conducted. Thus, a low contamination level (O₂ \approx 20 ppm and H₂O \approx 100 ppmV) is maintained and controlled using a Cambridge Sensotec Rapidox 3100 gas sensor.

Four different gas mixtures were used for the Micromegas stability studies: Ar-CO₂ 90-10, Ar-CO₂ 70-30, Ne-CO₂ 90-10, and Ne-CO₂ 70-30. Argon and neon were chosen due to their properties as noble gases. They have low electron attachment and are chemically non-reactive. Furthermore, they don't have any rotational or vibrational states. Through

these, gases could absorb electron energies and therefore increase the onset voltage of avalanche multiplication. Some relevant properties are listed in table 3.2. It is important to note, that some of these values (marked with *) are obtained through simulations with geometries that might differ from the ones given in these studies. However, they should provide a sufficient estimation.

	Ar-CO ₂ 90-10	Ar-CO ₂ 70-30	Ne-CO ₂ 90-10	Ne-CO ₂ 70-30
Density [10^6 g/cm ³]	1.8	1.84	1	1.22
Effective Ionization Energy [eV]	28.8	28.1	38.1	-
Primary Ionizations [1/cm]	25.42*	27.66*	14.35*	19*
Drift Velocity [cm/ μ s]	3.25	0.932	2.66	$\sim 1^*$

Table 3.2: Relevant properties of the different gas mixtures. With these, the dependency of gain and discharge probability on the used gas mixture can be explained. The values marked with * come from simulations, while the drift velocity was measured at normal ambient conditions (NPT) at a field of 400 V/cm. [36, 32]

Besides getting ionized, the noble gas atoms can also get excited by the traversing ionizing particle, leading to the eventual emission of UV photons. While these photons don't carry enough energy to ionize further gas atoms, they can create free charges on the metallic surfaces of the detector through the photoelectric effect. Additionally also ions themselves can possibly emit UV photons or extract additional electrons when neutralizing at the cathode. These free charges then potentially lead to additional electron avalanches in different places. Therefore CO₂ is added as quencher gas, mitigating the mentioned processes by absorbing UV photons through its rotational and vibrational states or by exchanging charge with the ionized noble gas. The motivation for choosing exactly the before mentioned gas components and ratios is more practically natured, as these are commonly used in the MPGD community.

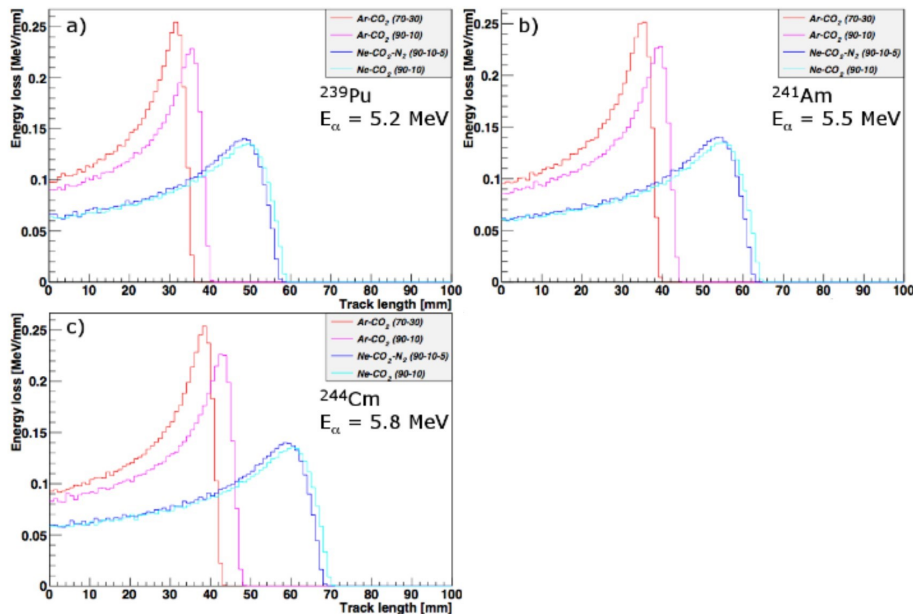


Figure 3.4: Simulated Bragg curves of the components of the mixed alpha source in three of the gas mixtures used for this thesis. The energies correspond to averaged values. The different charge densities created along the trajectory of the particles become clear. [37]

In figure 3.4 the Bragg curves of alpha particles with different energies, comparable to the components of the alpha source used in this study are shown for different gas mixtures. As can be seen, the maximum drift distance achieved by those alpha particles depends largely on the used gas mixture, as the energy loss is directly proportional to the gas density. The maximum energy is deployed at the so-called Bragg peak.

3.2 Measurement Procedures

Gain

One of the major performance factors of MPGDs is the gain. It provides a measure of the achieved signal amplification and is defined as the ratio of electrons collected on the anode N_{and} to electrons created in the primary ionization process N_{prim} . Effectively, the gain is measured as the amplified anode current I_{and} , divided by the current created through the initial ionization process, the so-called primary current I_{prim} . The primary current gets measured without any amplification field applied, hence it can be assumed, that the created primary electrons either are collected on the micro-mesh or the anode. The primary current thus gets obtained by addition of the mesh current and the anode current $I_{\text{prim}} = I_{\text{mesh}} + I_{\text{and}}$. To increase the accuracy, both mesh and anode are grounded during the measurement of I_{prim} .

$$G_{\text{abs}} = \frac{N_{\text{and}}}{N_{\text{prim}}} = \frac{I_{\text{and}}}{I_{\text{prim}}} \quad (3.1)$$

The gain is a function of the applied amplification voltage, showing an exponential behavior in the region of interest. However, mainly two things have to be taken into account when measuring the gain. Firstly, charge-up effects, which are a common process in MPGDs containing dielectric materials [38]. Charges can attach to insulating surfaces, due to transversal diffusion, eventually distorting the electric field and thus modifying the achievable gain. Therefore one has to wait several minutes (~5 min) after applying or increasing the amplification field until an equilibrium in the charge-up process is reached. Secondly, the current flowing during discharges hugely inflates the measured gain. To exclude this in the gain calculations, deviations larger than five sigmas with respect to the latest averaged current are ignored, basically cutting of the signals from discharges. The cutoff as well as the calculation of the running average are done by a Labview program, used to track and control the measurements.

Furthermore, the gain can be normalized to standard pressure and temperature (see equation (3.2)), as these parameters hugely influence the maximal achieved gain [39]. This way, gain results measured on different days can be compared more reliably. It is important to note, that the used normalization does not take into account any gas specific parameters.

$$G_{\text{norm}} = \left(\frac{1000 \text{ mbar}}{P} \right) \cdot \left(\frac{T}{20^\circ\text{C}} \right) \cdot G_{\text{abs}} \quad (3.2)$$

Discharge Probability

Discharge probability is used as the general measure of the discharge stability of MPGD based detectors. It is defined as the probability of an ionizing particle inducing a discharge

in the amplification gap of the Micromegas, hence it can be calculated by counting the number of discharges N_{dis} in a certain time period T , effectively obtaining a discharge rate R_{dis} , and dividing it by the rate of the radioactive source R_{source} (see equation (3.3)).

$$P_{\text{dis}} = \frac{N_{\text{dis}}}{TR_{\text{source}}} = \frac{R_{\text{dis}}}{R_{\text{source}}} \quad (3.3)$$

The discharge probability is studied as function of the gain. Therefore, a lower discharge probability at the same gain implies a higher discharge stability. The measurement time is set to $T = 20$ min for low discharge rates (around 10 discharges per 20 minutes) but is lowered for discharge counts above $N_{\text{dis}} = 200$, maximizing the obtained statistics while keeping the measurement duration at an acceptable level.

Ion Backflow

Ion backflow (IBF) influences the spatial resolution and the counting rate of MPGDs, as it distorts the drift field. Thus its suppression is of major importance. For example, the just recently upgraded ALICE TPC required the IBF to be below 1% at a gain of 2000, as otherwise the effect of the resulting field distortions would get too high for the desired operation rates of 50 kHz [40]. However, Micromegas show an intrinsic ion backflow suppression due to their special geometry and the resulting field configuration [2]. At high field ratios, Ion backflow values as low as $IBF = 1\%$ are commonly achieved by Micromegas. In turn though, higher applied electric fields also decrease the performance stability, thus compromises have to be made.

A first estimation of the IBF of the two used Micromegas is provided in this thesis by defining the IBF as cathode current I_{cat} divided by anode current I_{and} , studied as a function of the ratio of amplification field to drift field, the so called field ratio (equation (3.4)).

$$IBF = \frac{I_{\text{cat}}}{I_{\text{and}}} \quad (3.4)$$

3.3 Results

Gain

Figure 3.5 displays the measured gain curves of Micromegas 1 (640/15) as function of the applied amplification voltage $U_{\text{amplification}}$. The gain was measured at three different distances to the radioactive source: 47 mm, 31.5 mm and 21.5 mm and with four different gas mixtures: Ar-CO₂ 90-10, Ar-CO₂ 70-30, Ne-CO₂ 90-10 and Ne-CO₂ 70-30. The source distance d_{source} is calculated by adding the thickness of the cathode PCB plate (1.5 mm) to the respective drift gap d_{drift} . All gain measurements are normalized regarding ambient pressure and temperature using equation (3.2). While the precision of the high-voltage supply is assumed to be good enough to neglect the uncertainties, the errors of the gain are smaller than the symbols in Figure 3.5.

The first thing to notice is the strict exponential behavior of all curves in the high gain region ($G > 10^2$). This is as expected, whereas the low gain region, separated by a bend in the gain curve, shows some variances and a non-exponential behavior. In this region the gain is hugely influenced by other factors, such as gas contamination and humidity, causing the observed non-exponential behavior. However, this region is not of interest and thus

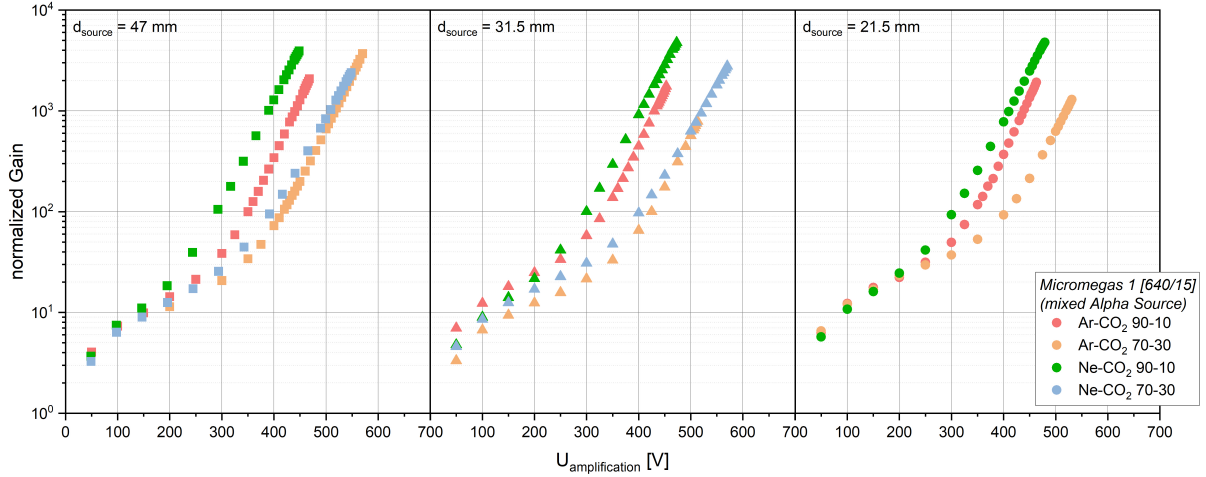


Figure 3.5: Measured gain curves of Micromegas 1 (640/15) for four gas mixtures and three source distances. The gain behaves exponentially in the region of interest ($G > 10^2$). The hierarchy regarding the gas mixture is explained by the lower effective ionization potential of argon and the admixture of quencher gas.

not taken into account for the studies presented in this thesis. The second thing to notice is the hierarchy of the gain curves with respect to the used gas mixtures. The same order is observed for all three source distances. However, this observation is expected, as the same hierarchy was observed with other MPGDs like GEMs [32] and THGEMs [22]. It can be explained by looking at the Townsend coefficients of the two noble gases, argon and neon. Townsend described the avalanche multiplication process, observing dependencies on the used gases. As the Townsend coefficient of neon is higher than the one of argon, higher gains can be reached in neon based gas mixtures for the same amplification fields. The difference between 90-10 and 70-30 mixtures is explained by the increased amount of quencher gas, quenching the avalanche process and thus causing a decrease in gain.

The same Micromegas 1 gain measurements are depicted in figure 3.6, but sorted concerning the used gas mixture instead of the source distance. No conclusive differences between different source distances are observed, as the variations especially seen with the neon mixtures are too small and could be influenced by unknown or not controlled effects. Correspondingly, variations in the gain between different days and even different measurements on the same day are expected due to the high environmental influences. Thus the gain is expected to be independent of the source distance. This independence is necessary for particle detectors. Problems with particle identification would occur, as in addition to higher particle energies also their distance to the mesh would lead to higher retrieved signals.

In figure 3.7 the Micromegas 2 (730/13) gain measurements are presented, including the previously shown Micromegas 1 gain curves (see 3.5). Clear similarities regarding the hierarchy of gas mixtures, as well as the overall shape of the curves, are observed. Again, the variations in the gain curves are too small to clearly point towards differences in the gain behavior of both Micromegas. It therefore can be concluded, that the mesh geometries, 640/15 and 730/13, do not majorly influence the achieved gain. This stands in contrast to observations made before, where wire density and thickness hugely influenced the achieved gain [29]. However, the differences in mesh geometry of the two used Micromegas might just be too small. Thus, studies using Micromegas with more different geometries are required.

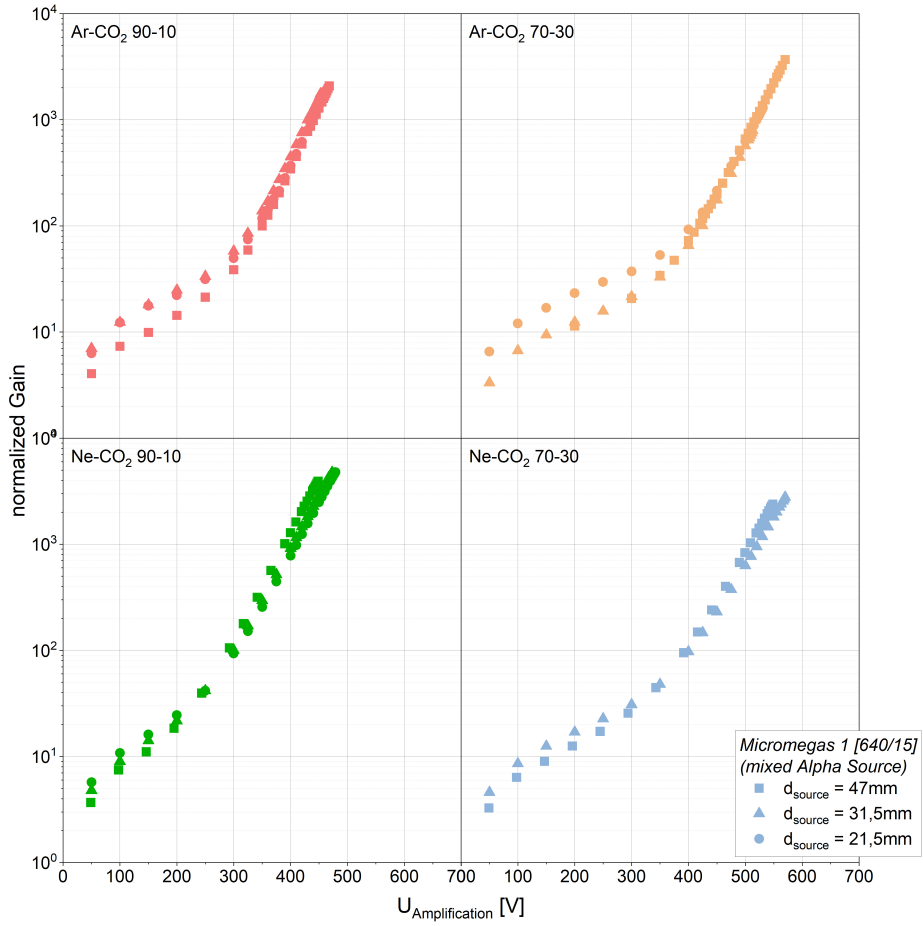


Figure 3.6: Same gain curves of Micromegas 1 (640/15) as in figure 3.5, sorted with respect to the used gas mixture. The differences for different drift gaps are too small to draw any conclusions.

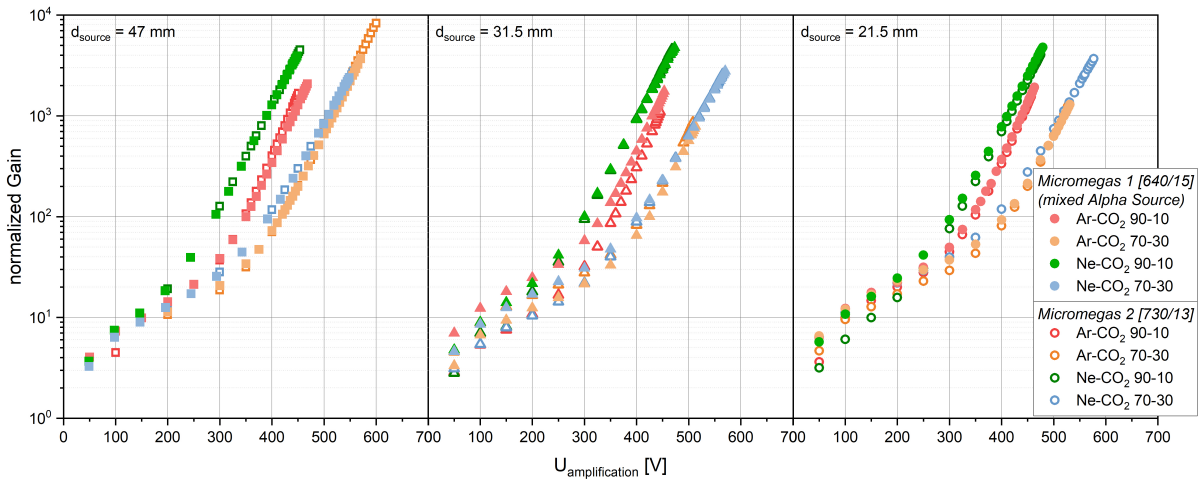


Figure 3.7: Comparison of gain curves of both Micromegas. Micromegas 2 (730/13) shows a similar gain behavior as Micromegas 1 (640/15). Again, the observed differences are too small to draw conclusions about a dependency on the different mesh geometries.

Discharge Probability

Figure 3.8 shows the measured discharge probabilities of Micromegas 1 with the four used gas mixtures, again sorted with respect to the source gaps. These measurements were done simultaneously to the gain measurements, thus each point in the discharge probability curve belongs to a point in the respective gain curve. Again, a hierarchy regarding the gas mixtures is observed, also similar to observations made with GEMs [32] and THGEMs [22]. For $d_{\text{source}} = 31.5$ mm and $d_{\text{source}} = 21.5$ mm, Argon based gas mixtures show a lower discharge stability than neon based ones. This is explained primarily by the lower effective ionization potential of Argon, thus more primary electrons are liberated by the ionizing particle. In addition, the range of alpha particles (see figure 3.4) is much shorter in argon than in neon. Combining these two properties, the number of primary electrons created per unit of length is much higher in argon based gas mixtures (see table 3.2). This eventually results in higher charge densities reaching the amplification region and thus increasing the probability of a discharge.

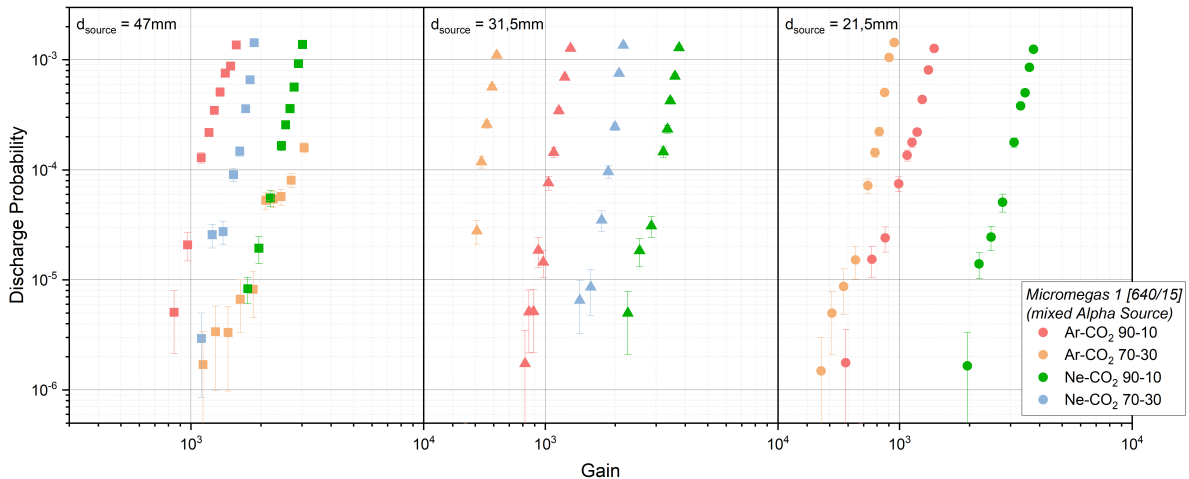


Figure 3.8: Measured discharge probability of Micromegas 1 (640/15) with four gas mixtures at three source distances. The observed hierarchy regarding the gas mixture is explained by the charge density reached in the amplification region. The different primary ionizations per centimeter (table 3.2) are the driving parameters. The different behavior for Ar-CO₂ 70-30 at $d_{\text{source}} = 47$ mm is explained by the range of alpha particles (figure 3.4) being below d_{source} , resulting in lower charge densities and thus a higher stability.

Secondly, the differences between 90-10 and 70-30 mixtures have to be looked at. Surprisingly, the gas mixtures with increased quencher proportions show a lower stability against discharges (again only looking at $d_{\text{source}} = 31.5$ mm and $d_{\text{source}} = 21.5$ mm). This is unexpected, as quenchers usually are added to increase the discharge stability admixture. However, the same effect used to explain the differences between argon and neon also applies to different quencher proportions, as the number of primary electrons per unit of length is higher for 70-30 mixtures (see table 3.2).

Adding to this, the plot for $d_{\text{source}} = 47$ mm requires further explanation. The probability curves show the same hierarchy observed with lower source distances, except for Ar-CO₂ 70-30, which shows a much higher stability. In addition, also the shape of the curve appears different than before, looking scattered and non-uniform especially for low probabilities. To explain this, one has to take a closer look at the range of alpha particles in Ar-CO₂ 70-30 compared to Ar-CO₂ 90-10. While the average range of alphas in Ar-CO₂ 90-10 is above 47 mm, the range in Ar-CO₂ 70-30 is slightly lower. Additionally, the energy distribution of alpha particles as a function of the traveled distance (Bragg curve, see figure 3.4) has its

peak near the maximum distance. As more energy is deployed in the region of the peak, higher charge densities are reached and thus discharges are more probable. However, also the spacing between peak position and amplification region has to be taken into account. Transversal diffusion causes the charge density to decrease over distance. Combining these observations, alphas in Ar-CO₂ 70-30 are stopped before they reach the mesh, resulting in lower charge densities inside the amplification region and thus inducing discharges less regularly. At higher gains though, the discharge curve looks stable again. An explanation could be that discharges now occur independent from high primary charge densities, but are caused by the increased avalanche multiplication due to the higher applied electric fields. Also small defects on the wires, enhancing the electric field, could now play a more important role [28]. For future references, these assumptions could be proven by measuring the discharge probability without a radioactive source inside the detector.

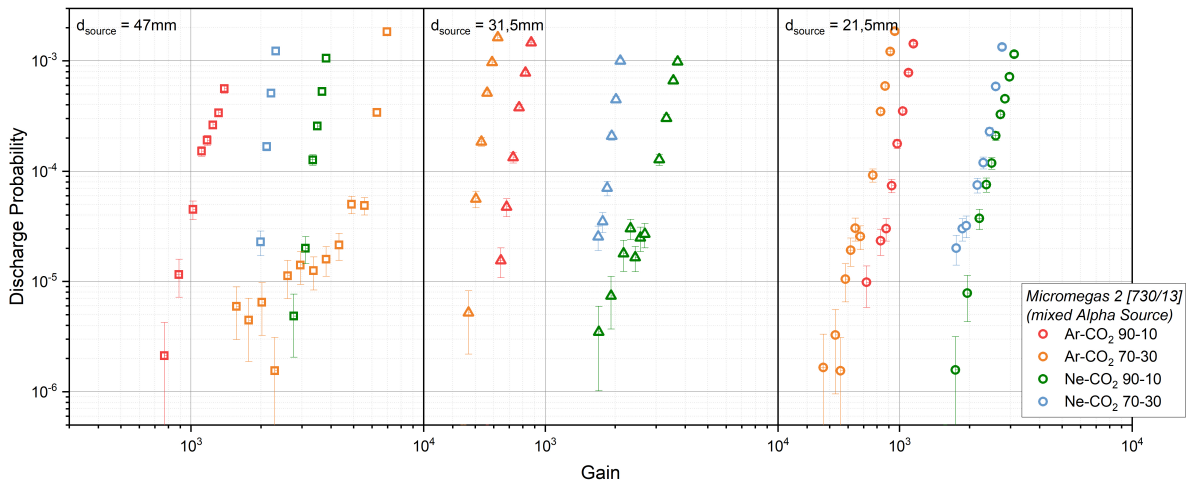


Figure 3.9: Measured discharge probability of Micromegas 2 (730/13) using four different gases at three source distances. The hierarchy and behavior regarding the gas mixtures is similar to the observations made with Micromegas 1 (640/15).

Figure 3.9 shows the measured discharge probabilities of the second Micromegas sample. The hierarchy of the measurements regarding the gas mixtures is exactly the same as observed with Micromegas 1. Again, argon based mixtures show a lower discharge stability, while 90-10 mixtures are more stable than 70-30 ones. Also the behavior in Ar-CO₂ 70-30 is similar, thus further confirming the assumptions made for Micromegas 1.

Finally, the influence of the source distance on the discharge stability has to be examined. For this, the same probability measurements conducted with Micromegas 1 are plotted, regarding the used gas mixture, in figure 3.10. Excluding the Ar-CO₂ 70-30 measurement at $d_{\text{source}} = 47$ mm, only slight dependencies on the source distance are observed. While the differences in argon based mixtures are not conclusive enough, neon based mixtures show a small, but visible decrease in stability for $d_{\text{source}} = 47$ mm. However, at low source distances the stability seems to be independent. A possible explanation is again provided by the shape of the energy distribution (figure 3.4). As the distribution shows an exponential behavior before reaching its maximum, the energy deployment doesn't increase as much at low track distances. Thus the charge densities created at $d_{\text{source}} = 21.5$ mm and $d_{\text{source}} = 31.5$ mm are more or less similar, resulting in similar discharge probabilities. As $d_{\text{source}} = 47$ mm is much closer to the energy peak, significantly higher charge densities are reached, causing the stability to decrease.

Also, the measurements conducted with Micromegas 2 are sorted with respect to the

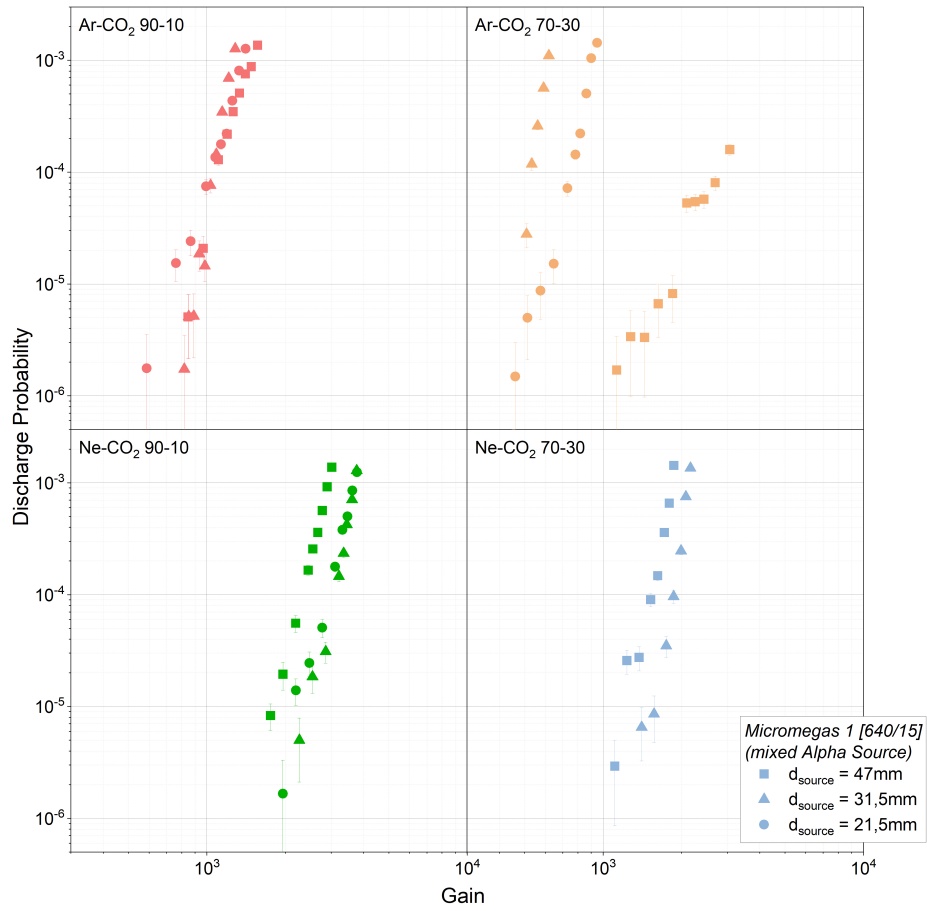


Figure 3.10: Discharge probability curves of Micromegas 1, sorted with respect to the used gas mixture. Except for the explained anomaly with Ar-CO₂ 70-30, the differences for the different source distances are too small and not understood well enough to draw any conclusions. Potentially, a dependency with neon based mixtures is observed, as these show a lower stability at $d_{\text{source}} = 47\text{mm}$.

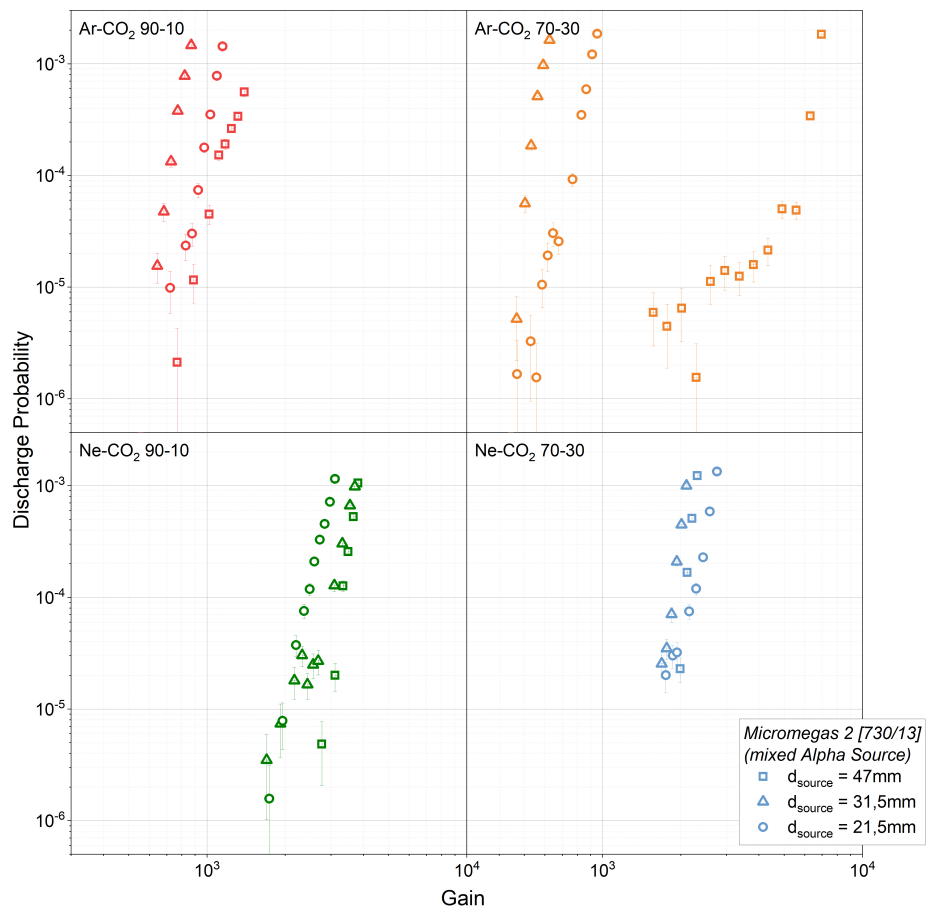


Figure 3.11: Discharge probability curves of Micromegas 2, sorted with respect to the used gas mixture. The potentially observed dependency for neon mixtures with Micromegas 1 now appears mixed-up. Thus, the variations regarding the source distance are too small and not understood well enough to draw any conclusions.

gas mixture, shown in figure 3.11. However, the observations made in figure 3.10 with Micromegas 1 do not hold up with Micromegas 2. While some gases, e.g. Ar-CO₂ 70-30, show a similar behavior, the hierarchy of neon based gas mixtures appears somehow mixed-up regarding the source distance, thus not supporting the assumptions made before. This points to other effects, that are either yet unknown or weren't taken into account. Therefore, more measurements at different source distances are needed before drawing solid conclusions about the dependency on the distance. The variations observed so far are too small and uncertain.

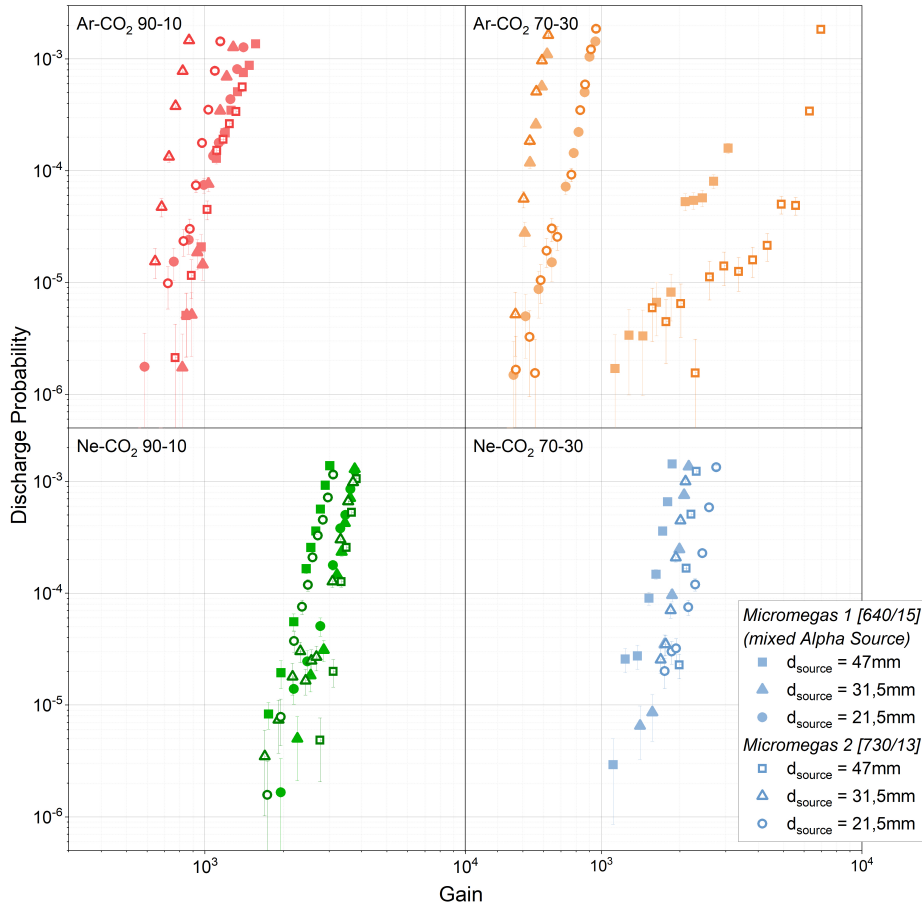


Figure 3.12: Comparison of discharge probability curves for both Micromegas, with respect to the used gas mixture. The differences are too small and not understood well enough to draw any conclusions about a dependency on mesh geometry. In the high gain region for Ar-CO₂ 70-30 at $d_{\text{source}} = 47 \text{ mm}$, the effect of charge density, caused by alpha particles, is assumed to be overshadowed by the charge density caused by avalanche multiplication. The now observed dependency on the mesh geometry was shown before under comparable conditions [29].

Figure 3.12 compares the discharge probabilities of both Micromegas. It again can be seen, that the general hierarchy of gas mixtures is similar for both meshes. The differences observed for the same gas mixtures at different source distances however cant be explained right now. The variances are either caused by yet unknown effects or factors not taken into account. These, for example, include the influence of increased electric fields caused by defects on single wires or non-uniformities of the wire intersections. In conclusion, the differences are too insignificant and not understood well enough to make any assumptions about the influence of the different mesh geometries.

Looking at Ar-CO₂ 70-30 for $d_{\text{source}} = 47$ mm, the curve stabilizes at much higher gains for Micromegas 2. This stabilization was assumed to be caused by the gain being high enough, so that avalanche multiplication itself is sufficient to create the charge densities needed for discharges. In comparison, measurements using a Fe⁵⁵ source, which creates much fewer electrons through initial ionization, showed a similar behavior: a higher stability was observed for meshes with higher wire density and smaller wire thickness [29]. This could therefore point towards a dependency on mesh geometry for low initial charge densities. For the high initial charge densities created by alpha particles, the mesh geometry is assumed to play a minor role for discharge stability, thus being negligible.

However, further studies have to be conducted. Especially geometrical simulations with different meshes are needed and already in planning, to get a better understanding and support the measured dependencies on gas, distance, and mesh geometry. One possible approach for such a simulation would look at single mesh "cells", consisting of only one hole and the surrounding wires. These cells would then get examined independently. Larger cells would collect a higher amount of charges due to their increased area, potentially reaching the critical charge limit faster. However, the achieved amplification field in the gap would probably be lower, leading to a higher charge limit. The overall performance of the Micromegas could then be characterized either by the performance of a single cell or by looking at the total number and area of the cells in the mesh. With such an analysis approach, more precise insights into the discharge formation mechanism and its driving factors for Micromegas are expected to be gained.

Ion Backflow

Figure 3.13 depicts the measured IBF of the two Micromegas, both conducted in Ar-CO₂ 90-10. It is important to note though, that these measurements are just an estimation, as for example, the cathode wasn't grounded when measuring its respective current, leading to relatively higher noise originating from the power supply. The IBF is plotted as a function of the field ratio. The observed anti-proportional behavior is as expected and was shown for Micromegas before [2]. The required low IBF at high gains is easily reached, as Micromegas 1 and 2 have backflow ratios of $IBF_1 = (1.1070 \pm 0.0002) \%$ and $IBF_2 = (1.1160 \pm 0.0002) \%$ respectively at a field ratio of $E_{\text{amp}}/E_{\text{drift}} = 84$. However, a clear difference between the two Micromegas is observed for lower field ratios, which could point to a dependency on the mesh geometry. However, previous measurements showed an increased IBF for lower wire densities, which is exactly the opposite of our observations [2]. Therefore one cannot draw any solid conclusions, as more accurate and in-depth studies have to be conducted.

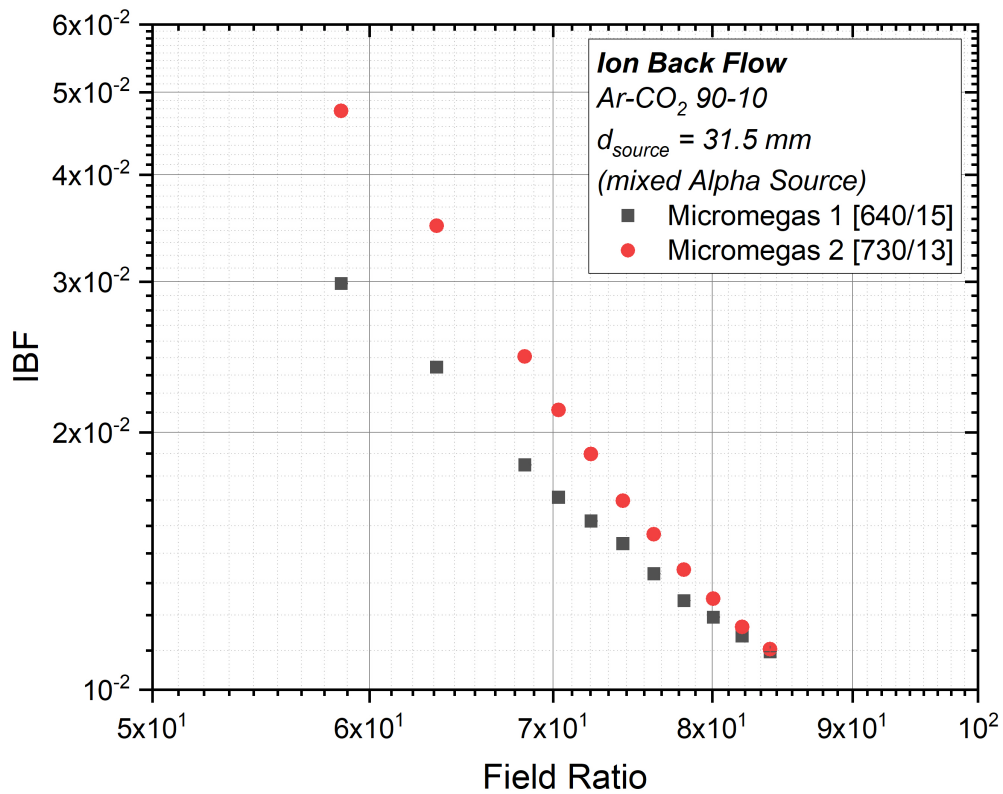


Figure 3.13: Measured ion backflow ratio of both Micromegas in Ar-CO₂ 90-10 at $d_{source} = 31.5 \text{ mm}$. IBF ratios of around 1% are reached at high gains. The observed dependency on the mesh geometry is contrary to observations made before [2]. However, the measurement is just an estimation, as for example the cathode wasn't grounded when measuring its current. Therefore a dependency on the mesh geometry cannot be concluded.

Chapter 4

Optical Discharge Studies with (TH)GEMs

4.1 Experimental Setup

The overall detector design for the optical discharge studies is similar to the design for the measurements with Micromegas. A scheme of it is shown in figure 4.1. Again, a gas-tight chamber was built, incorporating a supportive structure with cathode, (TH)GEM foil and anode mounted to it. To enable a line of sight between the spectrometer and the discharging (TH)GEM holes, a thin mesh anode with a transparency of 50 % was chosen. Furthermore, a BOROFLOAT window [41], transparent in the needed optical wavelength region, was integrated in the bottom side of the detector, facing the mesh anode. The spectroscopy studies were performed with an UV-VIS-NIR Ocean Optics QE65000 spectrometer. It is connected to the detector via a 600 μm optical fiber attached to a collimation lens. The lens in turn is mounted to the window on the bottom detector side, using a separate light-proof housing.

The same mixed ($^{239}\text{Pu} + ^{241}\text{Am} + ^{244}\text{Cm}$) alpha source used for the electrical discharge studies before was placed on top of the cathode. For the optical spectroscopy studies, the rate, measured over the 10 cm x 10 cm active area of a standard copper GEM, is 358 Hz. The emission rate differs from the rate measured with Micromegas, as it slightly depends on the effective radioactive area of the source. This takes the actual active area of the source itself, but also the area of the hole in the cathode into account. Thus, small variations in the position of the source with respect to the hole lead to differences in the effective alpha emission rate.

The drift and induction gaps were fixed at 27 mm and 2 mm respectively for all performed measurements. The top (TH)GEM electrode facing the cathode is connected to the independent multi-channel power supply unit with a 5 M Ω protection resistor. Additionally, 5 M Ω and 10 M Ω grounding resistors are attached to the top and bottom (TH)GEM electrodes to avoid over-voltages, caused by trips in the power supply and the consecutive ramp-downs.

For the main part of the measurements, either pure Argon (Ar 100) or Argon with a CO₂ proportion of 10 % (Ar-CO₂ 90-10) were used. The chamber was flushed with a rate of 10⁻³ m³/h, providing a constant exchange of the gas and maintaining an overpressure of 4 mbar with respect to the ambient atmospheric pressure. Further, impurities in the gas mixture, such as O₂ contamination or humidity (H₂O contamination) are again monitored.

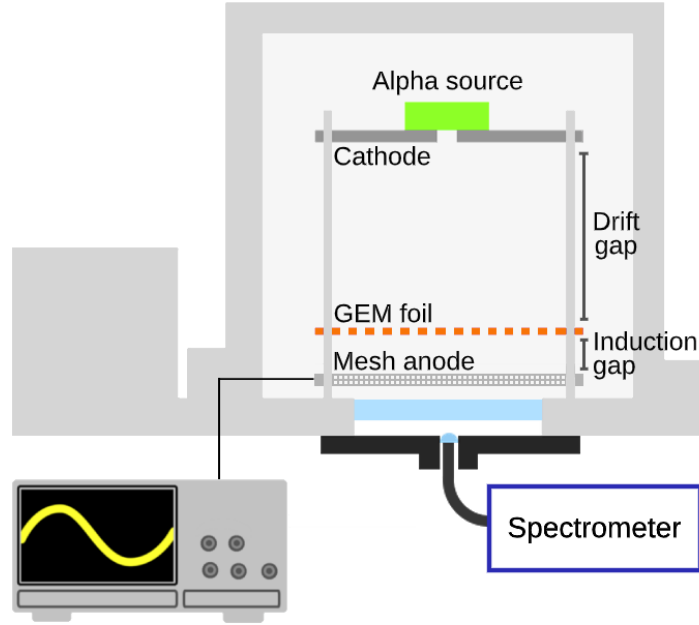


Figure 4.1: Scheme showing the detector chamber with its modifications for the spectroscopy measurements. Cathode, GEM foil, and mesh anode are mounted on supportive structures, the mixed alpha source is placed on top of the cathode. A window is built-in below the anode to enable the light collection by the spectrometer. The discharges are counted at the anode.

Exotic (TH)GEMs

Several different GEM and THGEM foils were used in our studies, all produced with different materials for the conductive cladding layer as electrodes of the foils. As the smaller scale of standard GEMs complicates production, only copper and aluminum GEMs were produced. For THGEMs however, foils with more "exotic" materials, being stainless steel (Inox), molybdenum, tantalum, and tungsten were provided in addition to copper and aluminum (see figure 4.2).

The used GEM foils are thin, 50 μm thick poly-amide foils with a 5 μm thick copper or aluminum cladding on both sides. Holes are etched into the foil in a hexagonal pattern with a standard pitch of 70 μm . As the etching takes place on both sides, the results are double conical shaped holes with an inner diameter of 50 μm and an outer diameter of 140 μm . The active area amounts to 10 cm x 10 cm.

The provided "exotic" THGEMs are 800 μm thick foils, while the cladding layer amounts to 25 μm (*50 μm for tungsten). They have a 10 cm by 10 cm active area. However, they are so-called single hole THGEMs (sh-THGEMs), having only one hole, 400 μm in diameter, for amplification in the middle of the foil. This ensures a constant light intensity per discharge, as light emitted further away from the center would result in a lower intensity due to the longer distance to the lens. A huge disadvantage of sh-THGEMs is the not well-defined gain due to large parts of the conductive area not contributing to the amplification. However, this doesn't affect the primary discharge formation as these are caused by the charge density exceeding a critical limit inside the holes of the foils, thus mainly depending on the hole geometry [22].

The different materials were chosen to cover a wide range of material-specific properties, expected to possibly play a role in secondary discharge formation. A list of some of these properties is provided in table 4.1.

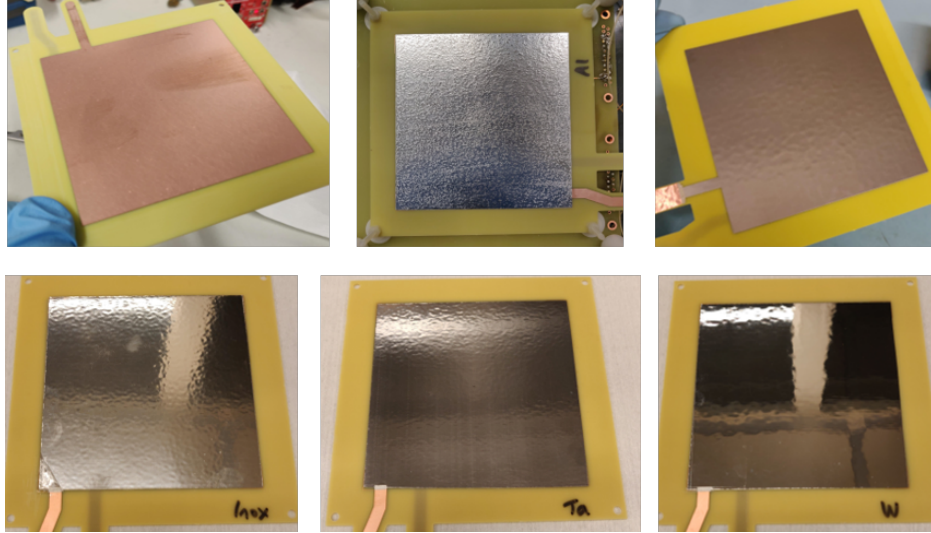


Figure 4.2: Pictures of the six different "exotic" sh-THGEMs. Upper row: aluminium, copper, Inox. Lower row: molybdenum, tantalum, tungsten.

Material	Conduc- tivity [$10^6 \frac{S}{m}$]	Work Function [eV]	Melting Point [$^{\circ}C$]	Boiling Point [$^{\circ}C$]	Thermal Conduc- tivity [$\frac{W}{m K}$]	Density [$\frac{g}{cm^3}$]
Al	36.9	4.08	660	2470	237	2.702
Cu	58.7	4.7	1083	2575	386	8.96
Inox	1.37	4.4	1510	2750*	16.3	7.85
Mo	18.7	4.5	2623	4651	138	10.22
Ta	7.6	4.22	3017	5365	57.5	16.65
W	8.9	4.5	3422	5550	174	19.35

Table 4.1: Relevant properties of the used cladding materials. Different hierarchies, regarding the materials, are observed for different parameters. * Value taken from Fe. [42, 43]

4.2 Measurement Procedures

Spectroscopy

The spectrometer is operated using the Oceanview software provided by the manufacturer. The exposure time during which the light from discharges is captured is relatively long. Measurements take up to 120 seconds, as the light emitted by a single discharge is very low. The exact exposure time was chosen to reach a certain amount of counts in the spectrometer. Further, a few iterations of every measurement are done, to average out background noise and decrease uncertainties. The background noise was hugely reduced by cooling the spectrometer with the built-in cooling system. Additionally, a background noise spectrum without any light emitted from discharges was taken as reference, to later get subtracted from the measured discharge emission spectra.

These, obtained by the described methods, raw spectra then got calibrated regarding their wavelength. For this, clear gas specific emission peaks in the discharge emission spectrum of the tungsten sh-THGEM measured in pure Argon were identified and fitted with a pseudo-Voigt function (equation (4.1)).

$$y = y_0 + A \left[m_u \frac{2}{\pi} \frac{w}{4(x - x_c)^2 + w^2} + (1 - m_u) \frac{\sqrt{4 \ln 2}}{\sqrt{\pi} w} e^{-\frac{4 \ln 2}{w^2} (x - x_c)^2} \right] \quad (4.1)$$

As the wavelength was calibrated before intensity, the used pseudo-Voigt fits were sufficient to get an exact peak position. A part of the spectrum is shown in figure 4.3, including the exponential background, the single fits as well as the cumulative total fit. However, not all fitted peaks were taken into account, as some couldn't get clearly associated or were too low in intensity. For example, the peaks at around 750 nm and 770 nm are expected to be double peaks, but only one fit was applied. The used peaks are marked with their respective, through fitting obtained wavelength. The actual wavelength values, taken from spectroscopy databases [44], are put in brackets. The wavelength then was corrected for the shift between the observed, fitted peak positions and the actual values.

Apart from the wavelength, also the intensity response got calibrated. The total experimental setup, including the spectrometer itself, the glass fiber, the lens as well as the window were calibrated with a deuterium lamp to correct the intensity distribution of the obtained spectra. This was done by comparing the original spectrum to the measured spectrum of the lamp, shown in figure 4.4. Simultaneously, also the scale was calibrated to a power density ($\text{Wm}^{-2}\text{nm}^{-1}$) instead of arbitrary units. On top of that, the intensity got normalized to a bin width of 1 nm.

All spectra were normalized to the number of discharges that occurred during the exposure time, thus the showed spectra can be understood as the light emitted by a single discharge. Further, some of the spectra presented in this thesis are normalized to the total integral over the relevant wavelength region from 270 nm to 975 nm. One reason being, that even after normalization to discharges, the overall recorded intensity still differed between different measurements of the same (TH)GEM samples. While slight differences in the gas contamination were observed to have no influence on the intensity, small variations in the position of lens and glass fiber were shown to play a role. This effect however was not taken into account while the measurements were conducted. Secondly, the used GEM foils are not single holed like the used sh-THGEMs. Therefore light emitted from

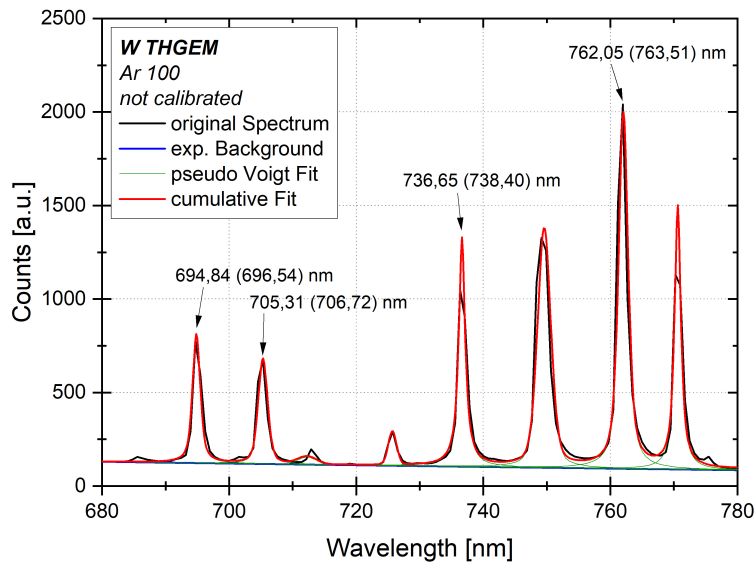


Figure 4.3: Pseudo-Voigt fits of a few gas peaks in the tungsten sh-THGEM spectrum in Ar 100. The original spectrum, the background fit, the single peak fits, as well as the cumulative peak fit is shown. By comparing the obtained positions of selected, distinct argon emission lines to values from spectroscopy databases (in brackets) [44] a wavelength calibration can be conducted.

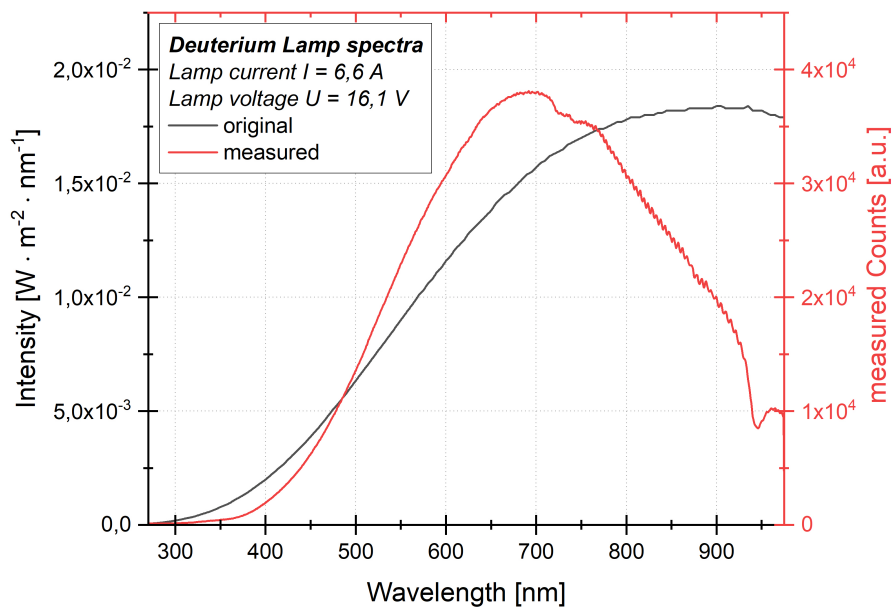


Figure 4.4: Original and measured spectra of the deuterium calibration lamp. By comparing these, an intensity calibration can be done. The whole setup, including window, lens, glass fiber and spectrometer was calibrated.

discharges in holes farther away from the lens resulted in a lower intensity measured by the spectrometer, lowering the total measured intensity. After integral normalization, GEMs and sh-THGEMs as well as different measurements in general can now be compared to each other regarding the relative heights of the emission lines.

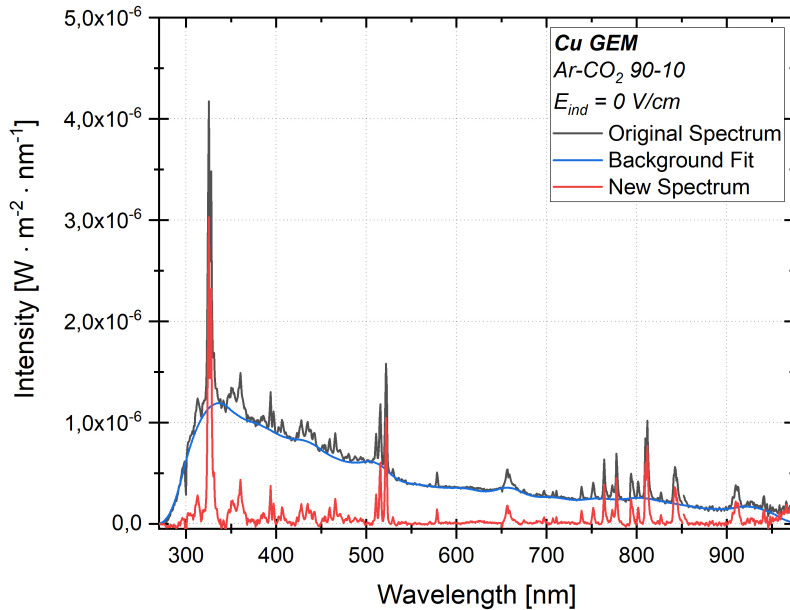


Figure 4.5: Process of background fit and subtraction, shown with a standard copper GEM spectrum in Ar-CO₂ 90-10. The background mainly comes from molecular emission bands and therefore is not of interest for the studies in this thesis [45]

Finally, a background fit was done, using a software provided by C.M. Galloway, E.C. Le Ru, and P.G. Etchegoin [46]. In their respective paper, further insights into the process and its underlying mathematics are presented. The result of the process, including the original spectrum and background fit as a reference, is shown in figure 4.5, using a copper GEM Ar-CO₂ 90-10 emission spectrum as an example. This background mainly originates from molecular emission and absorption processes by the quencher and contamination molecules. In figure 4.6 the spectra of an aluminum sh-THGEM measured in pure Ar 100 and Ar-CO₂ 90-10 are compared. To show the major background differences, the Ar 100 spectrum is scaled down by $1/3$, so that the gas specific emission lines in the high wavelength region have similar intensities. Thus, the effect of the quencher gas can be clearly seen. As these molecular emission bands are more complicated and are of minor importance for the studies in this thesis, the fitted respective background is subtracted from all spectra, which now only show the characteristic gas and material emission lines.

Secondary Discharges

Similar to primary discharges, the stability against secondary discharges is measured by counting the number of primary N_{dis} and secondary discharges N_{sec} at different induction fields. Thus, the secondary discharge probability can be defined as their respective ratio (see equation (4.2)). The measurement is conducted by applying a certain amplification voltage, causing discharge rates of around $R_{\text{dis}} \approx 1$ Hz. Then the induction field is increased

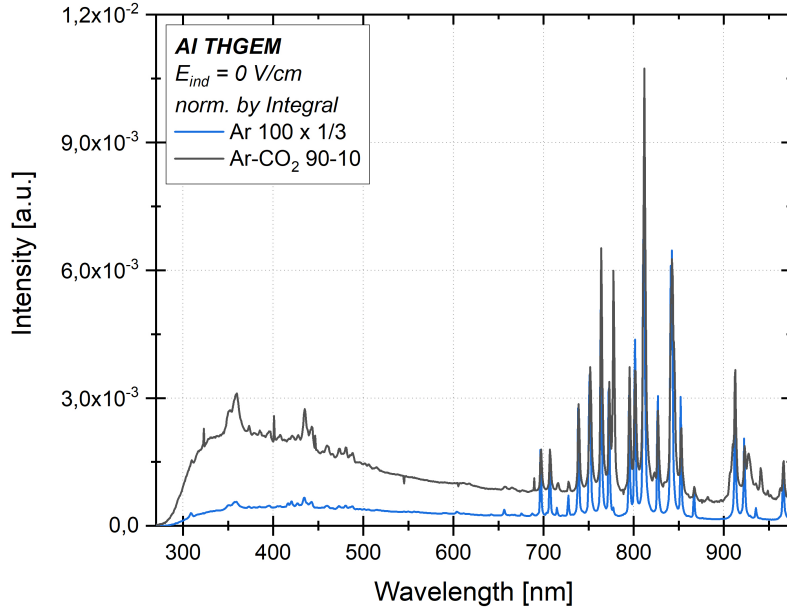


Figure 4.6: Comparison of aluminum sh-THGEM spectra measured in Ar 100 and Ar-CO₂ 90-10. The Ar 100 spectrum is scaled down, so the gas specific emission lines match in intensity. Now the background originating from molecular bands is clearly seen.

gradually, until a secondary discharge probability of $P_{\text{sec}} = 1$ is reached. The obtained probabilities are commonly plotted as a function of the applied induction field.

$$P_{\text{sec}} = \frac{N_{\text{sec}}}{N_{\text{dis}}} \quad (4.2)$$

4.3 Results

Spectroscopy

In figure 4.7 the edited (see section 4.2) spectrum of a standard copper GEM is shown. The measurement was done in Ar-CO₂ 90-10, thus one can clearly see the gas specific emission lines from Argon and Oxygen, especially in the long wavelength region. Characteristic lines of CO₂ cannot be distinguished, especially as the rotary and vibration states have characteristic lines mainly in the infrared region [45]. Furthermore, other contaminations of the gas mixture such as humidity are observed in the form of characteristic H₂ emission lines.

Most important though are the dominating material-specific lines from copper, especially in the low wavelength region around 400 nm. The observed clear and thin lines cannot come from copper atoms contained in the crystal lattice of the cladding layer, as this would result in broad emission bands instead. As such, it can be concluded that the observed emission lines originate from free copper atoms in the discharge plasma. This points to the evaporation of the cladding material during primary discharges. Matching this observation, evaporation of foil material was previously expected, as the copper layer around the hole was shown to get damaged during discharges [47].

Additionally, the spectrum of an aluminum GEM was measured in Ar-CO₂ 90-10. In

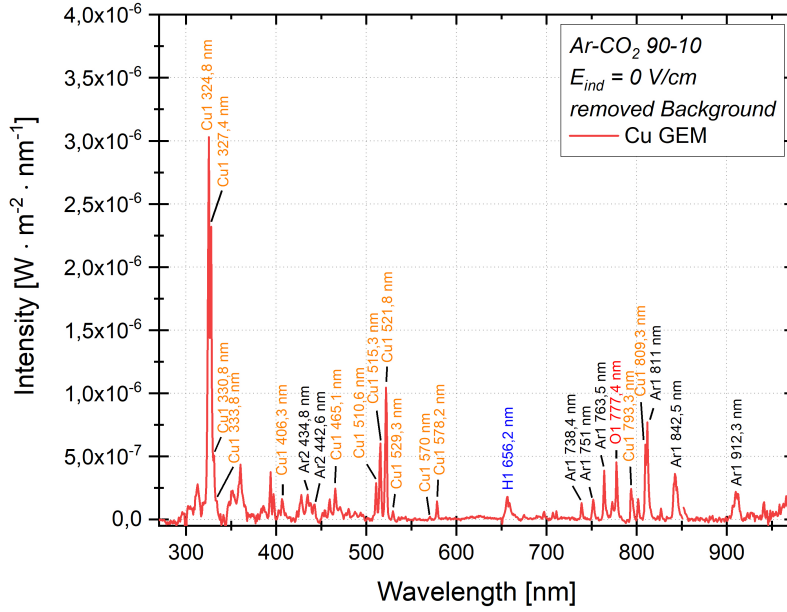


Figure 4.7: Measured optical emission spectrum of primary discharges with a standard copper GEM foil in Ar-CO₂ 90-10. The spectrum is dominated by material-specific emission lines, especially in the low wavelength region. This points towards evaporation of foil material due to the heat created during primary discharges. In addition, also gas-specific lines and peaks from gas contaminations (H₂) are observed.

figure 4.8 the emission spectra of copper and aluminum GEMs are compared. While the characteristic gas peaks show similar intensities, the low wavelength region is now dominated by aluminum specific lines instead of copper lines, which isn't unexpected as the evaporation temperature of aluminum is lower than that of copper (see table 4.1). This confirms the correct association of observed peaks with material and gas specific emission lines.

To make a safe conclusion, more than two foil materials would be needed for the studies, but due to the mentioned difficulties of GEM production only aluminum and copper GEMs were available. Sh-THGEMs, however, are much more easy to produce and thus foils with four additional materials, stainless steel (Inox), molybdenum, tantalum, and tungsten were provided.

Sh-THGEM cladding material	Onset voltage of primary discharge formation [V]
Al	1690
Cu	1680
Mo	1700
Inox	1685
Ta	1700
W	1683

Table 4.2: The stable operation limit for the used sh-THGEM foils. As a gain cannot be defined for sh-THGEMs, the limit is estimated by the onset voltage of primary discharges.

The onset voltages for primary discharges for each foil are listed in table 4.2. Assuming the

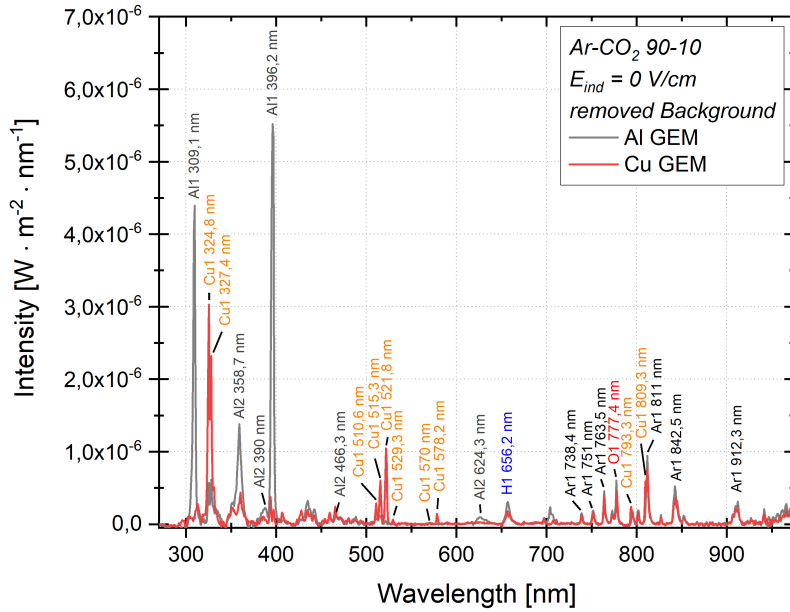


Figure 4.8: Comparison of discharge spectra from aluminum and copper GEM foils, measured in Ar-CO₂ 90-10. Instead of copper emission lines, aluminum lines are observed in the aluminum spectrum, confirming the correct association of the peaks.

gain is similar for similar voltages, with slight differences due to variations in temperature and pressure, the different sh-THGEM foils appear to have a similar primary discharge stability with respect to the cladding material. Thus primary discharge formation is shown to be independent of the foil material.

Before looking into the differences between sh-THGEMs, first, the different foil geometries of GEMs and sh-THGEMs have to be studied regarding their effect on the emitted light.

Thus, spectra of GEM and sh-THGEM foils with aluminum and copper are compared in figure 4.9. The first thing that strikes the eye are the much more pronounced gas-specific lines of both sh-THGEM spectra in the high wavelength region. Surprisingly though, none of the material-specific lines are visible. This leads to the conclusion that either negligibly low quantities or no foil material at all was evaporated during primary discharging, which in turn implies that the required high temperatures for evaporation aren't reached in sh-THGEMs. It is anticipated, that the higher and faster heat dissipation of the thicker cladding layer limits the reached temperature.

In figure 4.10 the emission spectra of all six different sh-THGEMs are shown. While the characteristic gas lines are similar for all foils, no specific lines are visible for any of the materials. As secondary discharges are observed for all sh-THGEM foils (see figure 4.12), it is concluded that the evaporation of foil material doesn't play a leading role in secondary discharge formation. Additionally, this could point towards thermionic electron emission being independent of the heat created during discharges, but instead being primarily influenced by other, yet unknown effects. However, evaporated material still could affect the overall stability against secondary discharges. As sh-THGEMs don't show any material evaporation, further research with different standard GEM cladding materials would have to be done.

Lastly, the emission spectra of secondary discharges are examined. As secondaries always

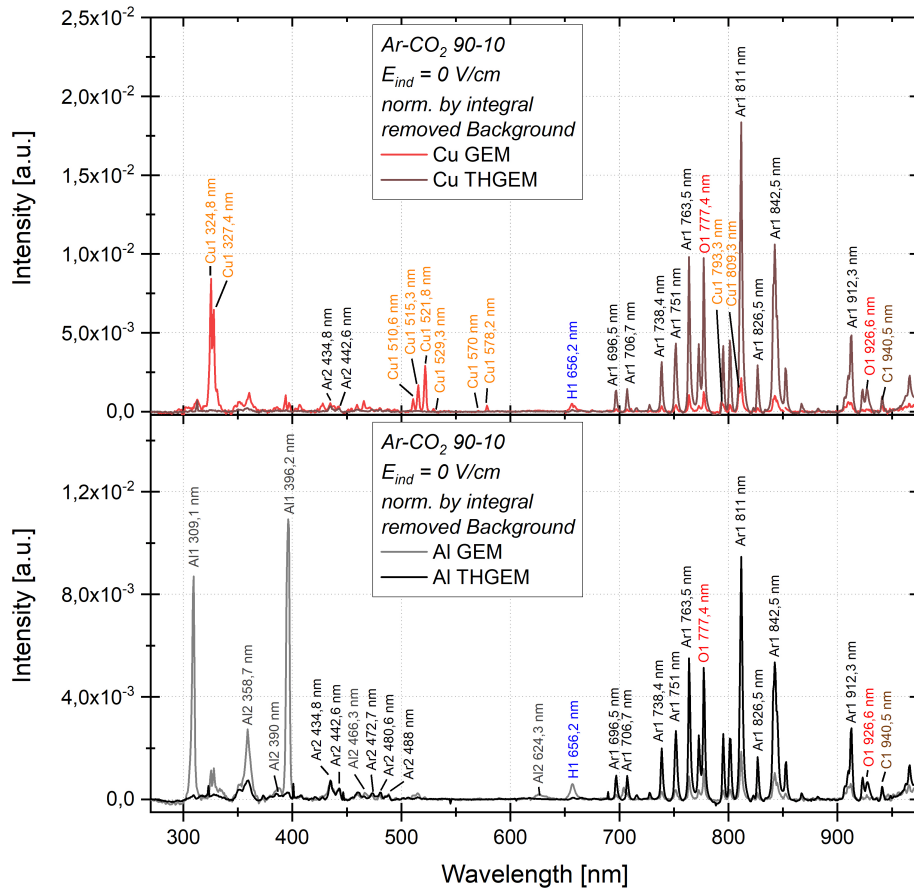


Figure 4.9: Comparison of discharge spectra of GEMs and sh-THGEMs for copper (top) and aluminium (bottom). The sh-THGEM spectra are dominated by gas specific emission lines in the high wavelength region, whereas no material peaks are observed. Due to the higher heat capacity of the thicker cladding material, the necessary temperatures for evaporation are not reached during discharges.

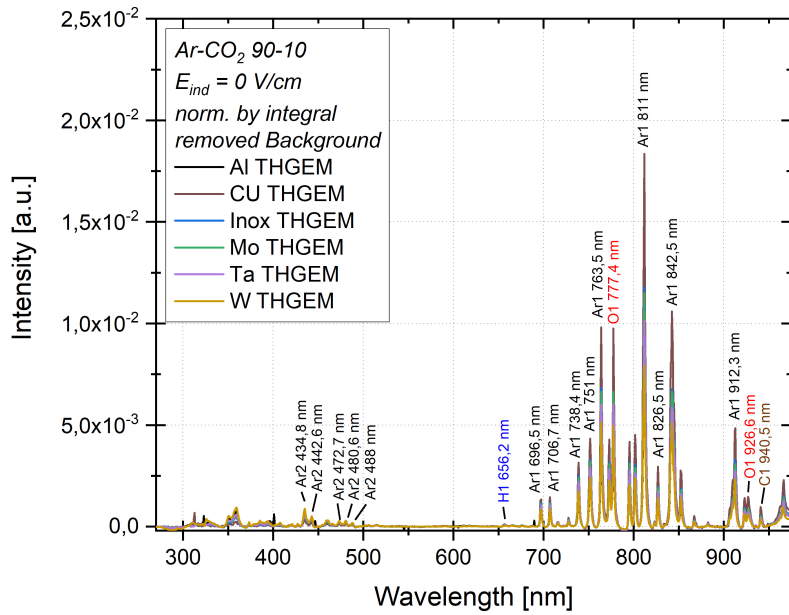


Figure 4.10: Comparison of discharge spectra for all six different sh-THGEM foils in Ar-CO₂ 90-10. No specific lines are observed for any of the materials. As secondary discharges still occur in sh-THGEMs, evaporated foil material is not expected to play a leading role in secondary discharge formation.

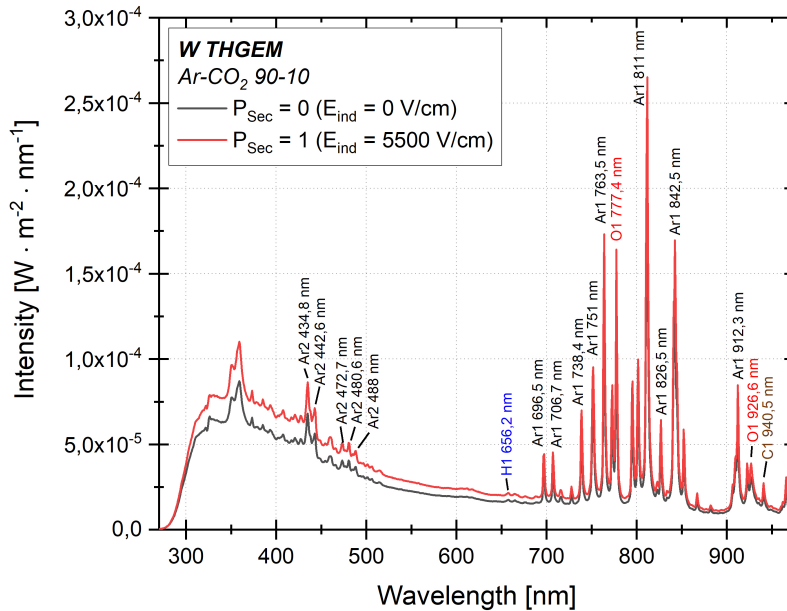


Figure 4.11: Primary and secondary emission spectra of a tungsten sh-THGEM in Ar-CO₂ 90-10. A slight increase in intensity is observed due to the additional light emitted by the secondary discharges. No additional characteristic lines are observed, pointing towards similarities in the light emission process for both discharge types.

emerge after a primary, with a time delay of a few tens of microseconds, it isn't possible to solely measure the secondary discharge emission spectrum with the used methods. Therefore, the proportion of secondary discharge light is maximized, by measuring at a secondary discharge probability of $P_{\text{sec}} = 1$. The obtained total spectrum of a tungsten sh-THGEM, measured in Ar-CO₂ 90-10 at an induction field of 4000 V/cm is compared to its primary discharge emission spectrum in figure 4.11. An increase in intensity is observed as a result of the additional discharges, but material-specific lines still aren't visible. On the one hand, this again confirms, that evaporated foil material does not take part in the secondary discharge formation process or at least isn't required. On the other hand, this points towards similarities in the light emission process, which appears to be independent of the formation mechanism of primary and secondary discharges.

Secondary Discharge Stability

The secondary discharge probabilities were measured with all six sh-THGEMs, shown in figure 4.12. An additional copper sh-THGEM measurement was added as a reference, to show expected variances for similar materials. Thus, clear dependencies on the cladding material are observed, as especially molybdenum stands out with a much higher stability. However, comparing this hierarchy to material-specific properties such as work function, conductivity, or boiling point (see table 4.1), no similarities are observed. On top of that, molybdenum does not stand out in any of the listed categories. This is surprising, as especially the work function hugely influences the thermionic electron emission, which is assumed to be a driving factor in secondary discharge formation [34, 33]. Comparing this measurement to the observations made with spectroscopy, also the boiling point as a factor can be excluded. A dependency on the boiling temperature would mainly be expected, when evaporation of the cladding material takes place, which it does not in the case of sh-THGEMs (see figure 4.10). It thus can be concluded that evaporated foil material is not crucial for the underlying secondary discharge formation mechanism and the overall stability against these discharge events. Further, the observed primary discharge stability (table 4.2) being similar for all materials points towards different formation mechanisms for primary and secondary discharges.

As major material properties do not seem to affect the secondary discharge stability of sh-THGEMs in a straightforward way, it would be of interest, to examine the effects of hole geometry or surface properties, such as porosity. While the hole geometry, studied with an optical microscope, showed no clear dependencies, an electron microscope would be needed to get further insights on the cladding surface, as especially its porosity is expected to play a major role in thermionic electron emission. Also, GEMs with more different cladding materials are needed for investigations regarding their secondary discharge stability but also their discharge emission spectra. These would help to get an understanding of the actual influence of evaporated foil material on secondary discharge stability, as this could not be shown with sh-THGEMs.

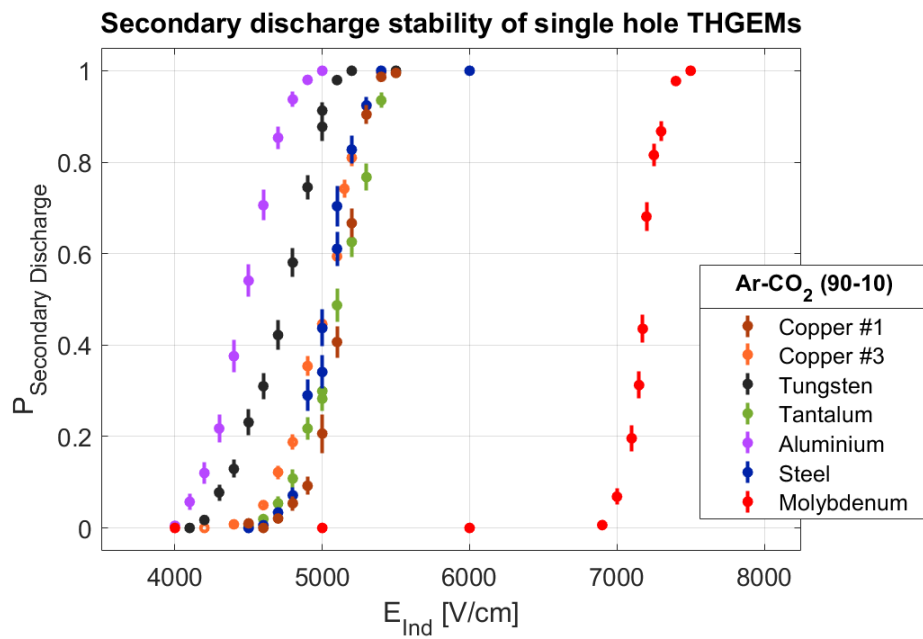


Figure 4.12: Measured secondary discharge probability of the six "exotic" sh-THGEMs. A second copper measurement is added as a reference, to show variances for similar materials. A material dependency is observed, as especially molybdenum is standing out. However, this cannot be explained by major material properties (table 4.1), pointing to yet unknown parameters and effects.

Chapter 5

Summary and Outlook

In the first part of this thesis, two Micromegas with different mesh geometries, (640/15) and (730/13), were tested regarding their gain and discharge stability. These important performance factors were measured using four different gas mixtures (Ar-CO₂ 90-10, Ar-CO₂ 70-30, Ne-CO₂ 90-10 and Ne-CO₂ 70-30) at three different distances to the radioactive source ($d_{\text{source}} = 47$ mm, $d_{\text{source}} = 31.5$ mm and $d_{\text{source}} = 21.5$ mm). The choice of gas mixture was shown to strongly influence the achieved gain and discharge stability, with Ne-CO₂ 90-10 showing the best performance in both categories, whereas no decisive conclusions about the dependencies on wire density, wire thickness, or source distance could be drawn. However, the results from these measurements align with observations made with GEMs [32] and THGEMs [22], thus confirming their accuracy. Still, further studies at more source distances are needed and planned to eliminate current uncertainties. Additionally, geometric simulations of the Micromegas setup are required to support the measured results and to obtain a better understanding of the underlying discharge formation mechanisms.

Furthermore, first measurements of the ion back flow were conducted, with more in-depth studies planned in the future. The IBF was shown to behave as expected, achieving ion backflow ratios around 1 %, needed for high rate particle detectors.

In the second part, GEMs and THGEMs with various cladding materials were studied. A total of six different materials, aluminum, copper, stainless steel, molybdenum, tantalum, and tungsten were provided for THGEMs, whereas only aluminum and copper GEMs were possible due to the more complicated production process. Spectroscopy methods were used, to investigate the light emitted during primary discharge events inside the holes of the foils. While material-specific emission lines were observed with normal GEMs, pointing towards evaporated foil material in the discharge plasma, these were absent in THGEM discharge spectra. In addition, also discharge stability studies were conducted with the different THGEMs. The primary discharge formation was shown to be independent of the foil material, conforming to expectations from the streamer discharge model. Concerning secondary discharges, delayed propagations of primary discharges inside the induction gap, significant material dependencies were observed, with especially molybdenum standing out. It exhibits a much higher secondary discharge stability than all other used foil materials. Combining this with the observations made through spectroscopy, evaporation of foil material is shown to not significantly influence secondary discharge formation in THGEMs. However, to also prove this for normal GEMs, further spectroscopy and discharge studies with more than two materials are needed. Additionally, the THGEM samples have to be investigated in more detail to uncover the mechanisms behind the molybdenum anomaly.

Acknowledgements

At first, I would like to thank Berkin Ulukutlu for his guidance, support, and help throughout this thesis, but also for interesting and humorous discussions as well as joyful times in the laboratory. Secondly, I want to thank Prof. Dr. Laura Fabbietti for giving me the great opportunity to work and study in her motivated and friendly group. Further, I want to thank Dr. Piotr Gasik for his nice advices, interesting comments, and helpful feed-backs during my work. Big thanks also to Lukas Lautner and Thomas Klemenz for their company and support, always happy to help. Here I also would like to thank all members of the whole E62 group, making this workspace a better place. Thanks also to Dr. Roman Gernhäuser for helping me with the radioactive source and for asking questions I did not think about. I also want to thank Sonja Winkler for her help with the microscopes. I would like to thank the EP-DT-DD Micropattern Technologies workshop at CERN for producing and providing the "exotic" (TH)GEMs, as well as the Micromegas used in this thesis. And finally, I wish to thank the RD51 community at CERN for their support and interest in these conducted studies.

Bibliography

- [1] Fabio Sauli. Principles of operation of multiwire proportional and drift chambers. In *Experimental Techniques in High-energy Nuclear and Particle Physics*, pages 79–188. World Scientific, 1991.
- [2] P. Colas, I. Giomataris, and V. Lepeltier. Ion backflow in the micromegas tpc for the future linear collider. *NIM A*, 535:226–230, 2004.
- [3] D. S. Bhattacharya, P. K. Sahu, S. Swain, and S. K Sahu. Preliminary results of ion backflow study for a single gem detector. 2017.
- [4] Y.L. Zhang, H.R. Qi, Z.W. Wen, H.Y. Wang, Q. Ouyang, Y.B. Chen, J. Zhang, and B.T. Hu. Spatial resolution measurement of triple-gem detector and diffraction imaging test at synchrotron radiation. 2017.
- [5] Y. Giomataris, Ph. Rebourgeard, J.P. Robert, and G. Charpak. Micromegas: a high-granularity position-sensitive gaseous detector for high particle-flux environments. *NIM A*, 376(1):29 – 35, 1996.
- [6] Fabio Sauli. Gem: A new concept for electron amplification in gas detectors. *NIM A*, 386(2-3):531–534, 1997.
- [7] I. Giomataris and G. Charpak. *NIM A*, 310:589, 1991.
- [8] P. Abbon and S. Aune. Micromegas for axion search and prospects. *Journal of Physics Conferences*, 65, 2007.
- [9] D. Thers, Ph. Abbon, J. Ball, Y. Bedfer, C. Bernet, C. Carasco, E. Delagnes, D. Durand, J.-C. Faivre, H. Fonvieille, A. Giganon, F. Kunne, J.-M. Le Goff, F. Lehar, A. Magnon, D. Neyret, E. Paschetto, H. Pereira, S. Platchkov, E. Poisson, and Ph. Rebourgeard. Micromegas as a large microstrip detector for the compass experiment. *NIM A*, 469:133–146, 2001.
- [10] B. Peyaud. Kabes: a novel beam spectrometer for na48. *NIM A*, 535:247–252, 2004.
- [11] I. Manthos, I. Maniatis, I. Maznas, M. Tsopoulou, P. Paschalias, T. Koutsosimos, S. Kompogiannis, Ch. Petridou, S.E. Tzamarias, K. Kordas, Ch. Lampoudis, I. Tsiafis, and D. Sampsonidis. The micromegas project for the atlas new small wheel. *AIP Conference Proceedings*, 2075, 2019.
- [12] F. Sauli and A. Sharma. Micropattern gaseous detectors. *Annual Reviews*, 49:371, 1999.
- [13] P. Bhattacharya, D. S. Bhattacharya, S. Mukhopadhyay, S. Bhattacharya, N. Majumdar, S. Sarkar, P. Colas, and D. Attie. Investigation of ion backflow in bulk micromegas detectors. *Jour. Instrm.*, 10, 2016.

- [14] C Altunbas, M Capéans, K Dehmelt, J Ehlers, J Friedrich, I Konorov, A Gandi, S Kappler, B Ketzer, R De Oliveira, et al. Construction, test and commissioning of the triple-gem tracking detector for compass. *NIM A*, 490(1-2):177–203, 2002.
- [15] M. Alfonsi, G. Bencivenni, W. Bonivento, E. Cardelli, A. Cardini, P. de Simone, D. Domenici, F. Murtas, D. Pinci, M. Poli Lener, D. Raspino, and B. Saitta. Production and performance of lhcb triple-gem detectors equipped with the dedicated cardiac-gem front-end electronics. *NIM A*, 572:12–13, 2007.
- [16] Lami S, Latino G, Oliveri E, Ropelewski L, Turini N and Totem Collaboration. A triple-gem telescope for the totem experiment. *Nuclear Physics B-Proceedings Supplements*, 172:231–233, 2007.
- [17] Münzer R and ALICE Collaboration. Upgrade of the alice time projection chamber. *NIM A*, 2019.
- [18] Fabio Sauli. The gas electron multiplier (gem): Operating principles and applications. *NIM A*, 805:2–24, 2016.
- [19] R. Chechik, A. Breskin, C. Shalem, and D. Mörmann. Thick gem-like hole multipliers: properties and possible applications. *NIM A*, 535(1):303 – 308, 2004. Proceedings of the 10th International Vienna Conference on Instrumentation.
- [20] A. Breskin, R. Alon, M. Cortesi, R. Chechik, J. Miyamoto, V. Dangendorf, J.M. Maia, and J.M.F. [Dos Santos]. A concise review on thgem detectors. *NIM A*, 598(1):107 – 111, 2009. Instrumentation for Colliding Beam Physics.
- [21] A. Breskin, M. Cortesi, R. Alon, J. Miyamoto, V. Peskov, G. Bartesaghi, R. Chechik, V. Dangendorf, J.M. Maia, and J.M.F. [dos Santos]. The thgem: A thick robust gaseous electron multiplier for radiation detectors. *NIM A*, 623(1):132 – 134, 2010. 1st International Conference on Technology and Instrumentation in Particle Physics.
- [22] L. Lautner. Influence of the charge density on discharges in thgem-based detectors. *Master Thesis*, 2019.
- [23] V Peskov and P Fonte. Research on discharges in micropattern and small gap gaseous detectors. *arXiv preprint arXiv:0911.0463*, 2009.
- [24] S Bachmann, A Bressan, M Capeáns, M Deutel, S Kappler, B Ketzer, A Polouektov, L Ropelewski, F Sauli, E Schulte, et al. Discharge studies and prevention in the gas electron multiplier (gem). *NIM A*, 479(2-3):294–308, 2002.
- [25] M. Vandenbroucke. Discharge reduction technologies for micromegas detectors in high hadron flux environments. *JINST*, 7, 2012.
- [26] EE Kunhardt and Y Tzeng. Development of an electron avalanche and its transition into streamers. *Physical Review A*, 38(3):1410, 1988.
- [27] D. S. Bhattacharya, R. Ströhmer, and T. Trefzger. A three-dimensional numerical model of discharge and its application in micromegas. *JINST*, 155, 2020.
- [28] D. S. Bhattacharya. A systematic numerical study on differetn micromegas for hv stability. *RD51 meeting September 2018*, 2018.
- [29] M. Alviggi, P. Iengo, M. Iodice, and G. Sekhniadze. Discharge behaviour of resistive micromegas. *NIM A*, 958:162359, 2019.

- [30] J. Bortfeldt. Development of floating strip micromegas detectors. *doctor thesis*, page 27, 2014.
- [31] Heinz Raether. Electron avalanches and breakdown in gases. 1964.
- [32] P Gasik, A Mathis, L Fabbietti, and J Margutti. Charge density as a driving factor of discharge formation in gem-based detectors. *NIM A*, 870:116–122, 2017.
- [33] A Deisting, C Garabatos, P Gasik, D Baitinger, A Berdnikova, MB Blidaru, A Datz, F Dufter, S Hassan, T Klemenz, et al. Secondary discharge studies in single-and multi-gem structures. *NIM A*, 937:168–180, 2019.
- [34] A Utrobicic, M Kovacic, F Erhardt, M Jercic, N Poljak, and M Planinic. Studies of the delayed discharge propagation in the gas electron multiplier (gem). *NIM A*, 940:262–273, 2019.
- [35] Eckert & ziegler nuclitec gmbh:, 2017.
- [36] Y. Assran and a. Sharma. Transport properties of operational gas mixtures used at lhc. 2011.
- [37] H. Appelshaeuser and W. Riegler. Addendum to the technical design report for the upgrade of the alice time projection chamber. *CERN-LHCC-2015-002 ; ALICE-TDR-016-ADD-1*, 2015.
- [38] J. Samarati, B. Alvarez Gonzalez, J. Bortfeldt, E. Maria Farina, P. Iengo, G. Sekhni-aidze, O. Sidiropoulou, and J. Wotschack. Study of the charge-up effect in micromegas detectors. *5TH INTERNATIONAL CONFERENCE ON MICRO-PATTERN GAS DETECTORS*, 2017.
- [39] J. Agarwala, M. Bari, F. Bradamante, A. Bressan, C. Chatterjee, A. Cicuttin, P. Ciliberti, M. Crespo, S. Dalla Torre, S. Dasgupta, B. Gobbo, M. Gregori, G. Hamar, S. Levorato, A. Martin, G. Menon, L.B. Rizzuto, Triloki, F. Tessarotto, and Y. X. Zhao. The high voltage system with pressure and temperature corrections for the novel mpgd-based photon detectors of compass rich-1. *NIM A*, 2019.
- [40] M. Ball, K. Eckstein, and T. Gunji. Ion backflow studies for the alice tpc upgrade with gems. *IOP Publishing*, 2014.
- [41] Andrew A Wereszczak and Charles E Anderson Jr. Borofloat and starphire float glasses: A comparison. *International Journal of Applied Glass Science*, 5(4):334–344, 2014.
- [42] G. N. Derry, M. E. Kern, and E. H. Worth. Recommended values of clean metal surface work functions. *JVST A*, 2015.
- [43] The engineering toolbox, 25.10.2020.
- [44] Physical Measurement Laboratory (NIST). Basic atomic spectroscopic data, 25.10.2020.
- [45] E. K. Plyler. The infrared emission spectra of co2 and h2o molecules. *Science*, 107:48, 1948.
- [46] C. M. Galloway, E. C. Le Ru, and P. G. Etchegoin. An iterative algorithm for background removal in spectroscopy by wavelet transforms. *Applied Spectroscopy*, 63, 2009.

- [47] J Merlin. Effect of discharges on gem detectors- single hole setup, 2018. Presentation in RD51 Collaboration Meeting 2018 Munich.